Cavitation pressure in water

Eric Herbert, Sébastien Balibar, and Frédéric Caupin
Laboratoire de Physique Statistique de l'Ecole Normale Supérieure associé aux Universités Paris 6 et Paris 7 et au CNRS, 24 rue Lhomond 75231 Paris Cedex 05, France
(Received 30 June 2006; published 16 October 2006)

We investigate the limiting mechanical tension (negative pressure) that liquid water can sustain before cavitation occurs. The temperature dependence of this quantity is of special interest for water, where it can be used as a probe of a postulated anomaly of its equation of state. After a brief review of previous experiments on cavitation, we describe our method which consists in focusing a high amplitude sound wave in the bulk liquid, away from any walls. We obtain highly reproducible results, allowing us to study in detail the statistics of cavitation, and to give an accurate definition of the cavitation threshold. Two independent pressure calibrations are performed. The cavitation pressure is found to increase monotonically from −26 MPa at 0 °C to −17 MPa at 80 °C. While these values lie among the most negative pressures reported in water, they are still far away from the cavitation pressure expected theoretically and reached in the experiment by Angell and his group [Zheng *et al.*, Science **254**, 829 (1991)] (around −120 MPa at 40 °C). Possible reasons for this discrepancy are considered.

DOI: 10.1103/PhysRevE.74.041603 PACS number(s): 64.60.Qb, 64.70.Fx, 64.30.+t

I. INTRODUCTION

The liquid and vapor phases of a pure substance can coexist at equilibrium only on a well defined line relating pressure and temperature. Away from this coexistence line, one of the phases is more stable than the other. However, because of the existence of a liquid-vapor surface tension, if one phase is brought in the stability region of the other, it can be observed for a finite time in a metastable state; the lifetime of this metastable state decreases as one goes away from the coexistence line. A detailed review about metastable states can be found in Ref. [1].

We are more particularly interested in the case where the liquid is metastable compared to its vapor. Such a state may be prepared in two ways: by superheating the liquid above its boiling temperature, or by stretching it below its saturated vapor pressure. We use the second method, and are able to reach negative pressures, that is, to put the liquid under mechanical tension. This allows us to study the nucleation of a bubble of the vapor phase, a phenomenon known as cavitation.

In this paper, we report our experimental results on cavitation in water. Water is a fascinating substance exhibiting many anomalies compared to other liquids. These anomalies arise mainly from the existence of a coordinated hydrogen bond network between water molecules. For instance, in the temperature region below the equilibrium freezing temperature (the liquid is then in a metastable state compared to the solid phase, a phenomenon called supercooling), several thermodynamical properties of liquid water exhibit a large increase in amplitude when the temperature is decreased. Several scenarios have been proposed to explain this behavior, however, experiments which would help to decide between them are hindered by the occurrence of crystallization. Motivated by this debate, we have decided to study cavitation in water, because it probes the cohesion between water molecules and can give information about the liquid structure; indeed, it was recently emphasized [2] that the knowledge of the temperature dependence of cavitation could help to put more constraints on the phase diagram of water.

Cavitation is easily favored by impurities, known as cavitation nuclei. This explains why cavitation is often observed close to equilibrium, and why results from different experiments are widely scattered. The influence of cavitation nuclei is more pronounced if large liquid volumes are studied over long time scales. The use of a focused ultrasonic wave allows us to study a tiny volume of bulk liquid without any wall, and during a short time. We measure the statistics of cavitation with greater accuracy than in previous studies, and obtain clearly defined and reproducible cavitation thresholds. The pressure calibration is checked by comparing two independent methods.

The paper is organized as follows. We first give a brief account of the theory used to predict the cavitation pressure in a stretched liquid (Sec. I A), and explain how the different scenarios of water lead to different temperature behaviors of the cavitation pressure (Sec. I B). We briefly review in Sec. II the various experimental techniques that have been developed to study this problem. In Sec. III, we give the details of our experimental methods, and emphasize the care taken to work with high purity water. Section IV details the methods of detection of cavitation events and of pressure calibration. This allows us to present in Sec. V the results obtained for the cavitation pressure and statistics, as well as their good reproducibility. The values found for the cavitation pressure disagree with theory: we finally discuss in Sec. VI the possible reasons for this discrepancy.

A. Theoretical background

We begin with a summary of the basic theory of nucleation [3–5]. Here we deal only with homogeneous cavitation in a bulk liquid, not with heterogeneous cavitation triggered on impurities or walls. In a liquid quenched at a pressure P below its saturated vapor pressure P_{sat}, the nucleation of the vapor phase represents a gain in energy, proportional to the

bubble volume. However, this nucleation process is hindered by the energy cost of the liquid-vapor interface. For a spherical bubble of vapor of radius R, the combination of these two terms writes

$$E(R) = \frac{4}{3}\pi R^3 (P - P_{\mathrm{sat}}) + 4\pi R^2 \sigma, \tag{1}$$

where σ is the liquid-vapor surface tension. This results in an energy barrier $E_b = (16\pi\sigma^3)/[3(P_{\mathrm{sat}} - P)^2]$ [at a critical radius $R_c = 2\sigma/(P_{\mathrm{sat}} - P)$] which has to be overcome for the bubble to grow spontaneously. Thermal fluctuations of the system can trigger nucleation, at a rate $\Gamma = \Gamma_0 \exp[-E_b/(k_B T)]$, where k_B is Boltzmann's constant and T is the absolute temperature. The prefactor Γ_0 is the product of the number density of nucleation sites by an attempt frequency for nucleation; it is often approximated by [6]

$$\Gamma_0 \simeq \left(\frac{4}{3}\pi {R_c}^3\right)^{-1} \frac{k_B T}{h}, \tag{2}$$

where h is Planck's constant. For an experiment performed in a volume V and during a time τ, the cavitation probability is $\Sigma = 1 - \exp(-\Gamma V \tau)$, and reaches $\frac{1}{2}$ at the cavitation pressure

$$P_{\mathrm{cav}} = P_{\mathrm{sat}} - \left(\frac{16\pi\sigma^3}{3k_B T} \frac{1}{\ln(\Gamma_0 V \tau/\ln 2)}\right)^{1/2}, \tag{3}$$

where P_{sat} is the saturated vapor pressure of the liquid at temperature T. One can see from Eq. (3) that the dependence of P_{cav} on $\Gamma_0 V \tau$ is weak, so that it can be considered as an intrinsic property of the liquid. A moderate error on Γ_0 will not affect the estimate of P_{cav}; hence the approximate Eq. (2) is sufficient. However, as a wide range of experimental parameters V and τ is available, we shall keep in mind this dependence when comparing different experiments (see Sec. II F).

This basic theory assumes that the energy of the bubble can be separated into a volume and a surface term [Eq. (1)], that is, that the thickness of the bubble wall (liquid-vapor interface) can be neglected compared to the bubble radius. We call this approach the thin wall approximation (TWA). The TWA is valid close to the coexistence line, but becomes a crude approximation at large negative pressures when the critical radius R_c becomes of the order of the interfacial width. For water at 300 K, and $V\tau = 1\ \mathrm{m}^3\ \mathrm{s}$, TWA predicts $P_{\mathrm{cav}} = -128$ MPa and $R_c = 1.1$ nm, close to the interface thickness (see Ref. [2] and references therein).

In addition to this oversimplification, TWA ignores a fundamental feature of any first-order transition: it possesses a spinodal limit. For a stretched liquid, this means that at a spinodal pressure P_s it ceases to be metastable and becomes macroscopically unstable. At P_s the liquid isothermal compressibility diverges and long-wavelength density perturbations grow without limit; this corresponds to a vanishing E_b. The existence of a spinodal line $P_s(T)$ where $(\partial P/\partial V)_T = 0$ is easily understood from the Van der Waals equation of state (EOS) for instance [1]; regardless of the EOS, it is a generic feature of all liquids.

A consistent theory of cavitation should thus improve TWA in two ways: (i) describe the nucleus of the new phase with a smooth profile between a low and a high density region; (ii) predict a vanishing nucleation barrier E_b on the spinodal line. This can be achieved within the frame of density functional theory (DFT) [1]. The precise choice of the EOS will affect the prediction for the cavitation pressure: we will now explain how this can help to constrain the theoretical description of water.

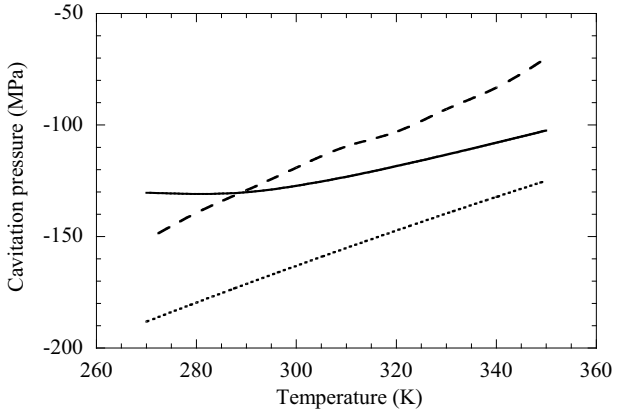

FIG. 1. Cavitation pressure in water as a function of temperature, calculated within the TWA (dotted line), or using DFT with Speedy's EOS (solid line) or with the TIP5P EOS (dashed line). The parameters used are $V = (10\ \mu\mathrm{m})^3$, $\tau = 1$ s, and Γ_0 given by Eq. (2).

B. Motivation of the study of cavitation in water

To explain the singular properties of supercooled water, three scenarios have been proposed. In 1982, Speedy [7] extrapolated isotherms measured at positive pressure to estimate the spinodal pressure; he obtained a spinodal line $P_s(T)$ with a minimum. Interestingly, Speedy showed that if the line of density maxima (LDM) of water reaches the spinodal line, thermodynamics requires that the slope of $P_s(T)$ changes sign at this particular point. As many properties are singular on $P_s(T)$, in order to explain water anomalies he proposed that $P_s(T)$ would retrace up to positive pressure in the supercooled region. On the other hand, Poole *et al.* [8] proposed that the spinodal remains monotonic (in their picture the LDM avoids the spinodal), and explained water anomalies by the vicinity of a new critical point, terminating the coexistence line between two (low and high density) metastable liquids; this scenario has been substantiated by all molecular dynamics simulations of water to date. A third scenario [9] proposed another consistent picture, where there is no second critical point, but where the increases in the response functions of water are simple thermodynamical consequences of its density anomalies.

Recently, two different EOS's illustrative of the first two scenarios were used along with DFT to predict the cavitation pressure in water [2]. The first EOS was proposed by Speedy [7] and shows a minimum in $P_s(T)$ ($\simeq -210$ MPa at 35 °C); the second EOS is calculated by molecular dynamics simulations using the five-site transferable interaction potential (TIP5P) [10] and leads to a monotonic $P_s(T)$. The results for the cavitation pressure are shown in Fig. 1. We can see that DFT results for P_{cav} are less negative than TWA results: this

is because for water, both the interfacial width and the critical radius for nucleation are around 1 nm. The main result is that the cavitation line $P_{cav}(T)$ exhibits the same qualitative behavior as the spinodal line $P_s(T)$, that is, with or without a minimum. This finding motivated our experimental investigation of the temperature dependence of P_{cav}. To measure the shape of $P_{cav}(T)$ is of course not sufficient to settle the question of the existence of the postulated second (liquid-liquid) critical point in water, but rather would provide a constraint that any overall picture of the phase diagram of water should be able to reproduce.

II. REVIEW OF THE PREVIOUS EXPERIMENTS

Observations of water and other liquids under tension were made as early as in the 17th century, as documented by Kell [11]. A detailed review of cavitation experiments is beyond the scope of this paper and can be found elsewhere [1,12–15]. The values of the cavitation pressure are amazingly scattered, even between similar experiments. In this section, we select for each different experimental method the reference giving the most negative value. This will serve as a benchmark for evaluation of our own method.

A. Berthelot tube techniques

This method, first employed by Marcellin Berthelot in 1850 [16], consists of the following. A vessel is filled with liquid water and sealed. If a gas bubble remains, the setup is warmed up until the bubble dissolves completely; from the dissolution temperature, the liquid density is deduced. The vessel is then cooled down, water sticks to its walls, and the pressure decreases, down to negative pressure if the temperature is low enough. The temperature at which cavitation occurs is measured, and the cavitation pressure is deduced using an extrapolated EOS. Corrections may be made for the thermal expansion of the vessel. This method can be improved by the use of an *in situ* pressure gauge: doing this, Henderson and Speedy found cavitation at −16 MPa at 38 °C [17] in glass capillaries (they also observed liquid water down to −20.3 MPa at 8.3 °C [18]), and Ohde's group reached a minimum value of −18.5 MPa at 53 °C [19] in metal tubes.

B. Centrifugation

This method, first employed by Reynolds [20], consists in rotating at high speed a tube containing water. Because of the centrifugal force, a negative pressure is developed on the rotation axis: $P=P_0-\frac{1}{2}\rho\omega^2 r^2$ where P_0 is the pressure outside the tube, ρ is the water density, and r is the distance between the center and the liquid-gas interface. The most negative value of P_{cav} was obtained by Briggs [21] with boiled distilled water in a Pyrex capillary tube. Briggs also investigated the temperature variation of P_{cav}: he found a minimum of −27.7 MPa at 10 °C, with $P_{cav}=-2$ MPa at 0 °C and −22 MPa at 50 °C.

C. Shock wave

Among cavitation experiments using shock waves, the one by Wurster *et al.* [22] is of particular interest. A weakly focused shock wave is further focused by reflection on a parabolic reflector. A fiber optic probe hydrophone measures the reflectivity of a laser beam at the fiber-water interface, from which the density of the liquid is deduced; the pressure is then estimated using an extrapolation of Tait equation of state for water [23]. With a rigid reflector, they find cavitation at −27 MPa on the hydrophone surface. On the other hand, with a soft reflector, they were able to reach "−59 MPa without cavitation at the fiber tip." They claim that "the reason for this is that the adhesion of water to clean glass is higher than the cohesion of water itself;" in fact, cavitation actually occurs away from the fiber tip [24]. As the study does not report any threshold for the onset of cavitation away from the tip, we will use the value −27 MPa for comparison (see Sec. II F), keeping in mind that this technique seems able to prepare liquid water at large negative pressures, at least close to the fiber tip.

D. Acoustic cavitation

An acoustic wave can quench liquid water to negative pressure (during its negative swing). Standing and traveling waves, focused or not, were used by many different groups. We will detail here the experiments by Galloway [25] and Greenspan and Tschiegg [26].

Galloway [25] used a standing wave produced by a spherical resonator. The sound amplitude at the center is measured with a piezoelectric microphone. Galloway defines the threshold for cavitation as the point "at which cavitation will occur at least once a minute, while a 10% reduction in the peak sound pressure will not produce any cavitation in a 15-minute interval." He found that P_{cav} varies from −0.1 MPa for distilled water saturated with air, to −20 MPa for distilled water degassed at 0.02% saturation. The way to define the threshold is of fundamental importance, because Galloway states that "pressure 100 times greater than this threshold pressure may be imposed on the sample for short lengths of time, of the order of seconds, without causing cavitation;" we also learn from Finch [27] that Galloway [28] "generally obtained much lower thresholds, of the order 1.5–2 MPa, with the higher values [−20 MPa] occurring only at certain times, there being no obvious explanation for the change." Galloway also noticed a small increase of P_{cav} with temperature (10% between 5 and 45 °C). Greenspan and Tschiegg [26] used a standing wave focused in a cylinder made of stainless steel to carefully study cleaned and degassed water. They calibrated P_{cav} by the static pressure method (see Sec. IV D) and found $P_{cav}=-16$ MPa (respectively, −21 MPa) for an average waiting time for cavitation of several minutes (respectively, seconds).

E. Mineral inclusions

The principle of this method is similar to the Berthelot tube method (see Sec. II A), except that it uses microscopic vessels. It deserves a separate paragraph because the most negative pressures reported in water were obtained with this method.

Water trapped in small pockets (in the 10–100-μm range) inside crystals can be found in nature. Angell and his group

TABLE I. Comparison between different cavitation experiments. Among the numerous and scattered values of the cavitation pressure in the literature, only the most negative have been selected.

Method	Ref.	T °C	V mm^3	τ s	$J=1/(V\tau)$ mm^{-3} s^{-1}	Wall	P_{cav} MPa
Berthelot	[17]	40	1	*20*	5×10^{-2}	Pyrex glass	−16
Berthelot	[19]	53	47	5	4.3×10^{-3}	stainless steel	−18.5
Centrifugation	[21]	10	*0.38*	10	2.6×10^{-1}	Pyrex glass	−27.7
Shock wave	[22]	25	*0.003*	10^{-8}	3.3×10^{10}	silica fiber	−27
Acoustic	[26]	30	200	0.1	5×10^{-2}	none	−21
Inclusions	[30]	40–47	4.2×10^{-6}	1	2.4×10^{5}	quartz	−140
Acoustic	this work	20	2.1×10^{-4}	4.5×10^{-8}	1.1×10^{11}	none	−24

used synthetic inclusions [29,30]. As their first paper deals with inclusions of saline solutions [29], we will focus on the second one where Raman spectra of the inclusions indicated a low salt concentration [30].

Crystals (quartz, calcite, and fluorite) are quench fissured in pure water between 300 and 400 °C. The fractured crystals are then sealed in Ag-Pd tubes with a known amount of ultrapure water, and autoclaved. During autoclaving, healing of the fissures traps water in inclusions at a desired density, depending on the autoclaving temperature and pressure. Angell and his group then followed Berthelot's method to study these inclusions: the bubble remaining in the inclusion disappears upon heating, at a temperature T_d; when the sample is cooled down, liquid water follows a nearly isochoric path, until cavitation occurs at T_{cav}. To deduce P_{cav}, they have to rely on an EOS: they chose to extrapolate the Haar-Gallagher-Kell (HGK) EOS to negative pressure. The HGK EOS is a multiparameter EOS fitted on data measured at pressures where the liquid is stable; it is qualitatively similar to Speedy EOS, but quantitatively different, giving for the coordinates of the minimum in the spinodal around 60 °C and −160 MPa.

For quartz inclusions, all inclusions in a given sample have the same T_d and hence the same density. There are two distinct cavitation behaviors. When $T_d>250$ °C (autoclaving temperature higher than 400 °C), T_{cav} is the same within ±2 °C for all inclusions in a given sample, whereas when $T_d<250$ °C (high density inclusions), T_{cav} is scattered. For fluorite and calcite, T_{cav} is always scattered, and the estimated P_{cav} is less negative that in quartz. Angell and his group attribute the scatter to heterogeneous nucleation, and its source to "possibly surfactant molecules cluster destroyed by annealing at the higher temperatures."

For low density inclusions in quartz, P_{cav} is positive, and compares well with the maximum temperature at which liquid water can be superheated, as measured by Skripov [31]. The maximum tension is obtained in one sample with high density inclusions (0.91 g mL^{-1} and $T_d=160$ °C); Angell and his group report that "some [inclusions] could be cooled to −40 °C without cavitation, and one was observed in repeated runs to nucleate randomly in the range 40 to 47 °C and occasionally not at all" [30]: they estimate nucleation occured at $P_{cav}\simeq-140$ MPa. The fact that "no inclusion that survived cooling to 40 °C ever nucleated bubbles during cooling to lower temperatures" was interpreted as an evidence that the isochore crosses the metastable LDM, thus retracing to less negative pressure at low temperature. This gives support to Speedy's scenario, at least in the sense that the LDM keeps a negative slope, deep in the negative pressure region in the P-T plane.

Further work on inclusions deals with the use of Brillouin scattering to measure the sound velocity in stretched liquid water [32]. This study reports tensions beyond −100 MPa at 20 °C. Additionally, it was able to show a volume change in a plateletlike inclusion, which points out the difficulty with the isochoric assumption made to estimate P_{cav}; on the other hand, for roughly spherical inclusions this assumption appears to be appropriate. It should be emphasized that in the work by Angell and his group, the inclusions in which they estimated $P_{cav}\simeq-140$ MPa "were not of well-rounded form, like those on which the reliable and reproducible high temperature data were obtained" [33].

To conclude with mineral inclusions, we shall mention a recent work focusing on kinetic aspects, by measuring the statistics of lifetimes of one inclusion at fixed temperatures [34]. The largest negative pressure achieved in this work is −16.7 MPa at 258.3 °C, and the lifetimes follow a Poisson distribution.

F. Comparison

Among the available measurements of the cavitation pressure in water, we select for each method those which give the most negative values. They are compared in Table I. We try to correlate the values to the parameter $V\tau$ which should affect the cavitation threshold as expected from nucleation theory (see Sec. I A). We define the experimental volume V (respectively, time τ) as the volume in (respectively, time during) which the pressure of the liquid is within 1% of its most negative value; when these quantities could not be inferred from the references, we used an arbitrary estimate (shown by an italic font). We also indicate the type of walls in contact with stretched water (if any), because of their possible effect on P_{cav}. We also give the values corresponding to our results at 20 °C; their measurement will be described in the following.

Figure 2 shows the cavitation pressure as a function of the quantity $J=1/(V\tau)$. For the sake of comparison, we have also

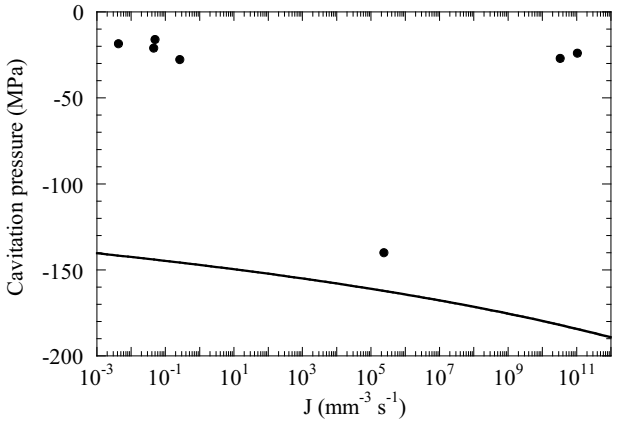

FIG. 2. Cavitation pressure as a function of the quantity $J=1/(V\tau)$. Data points are listed in Table I. The solid line is the prediction of the TWA [Eq. (3)].

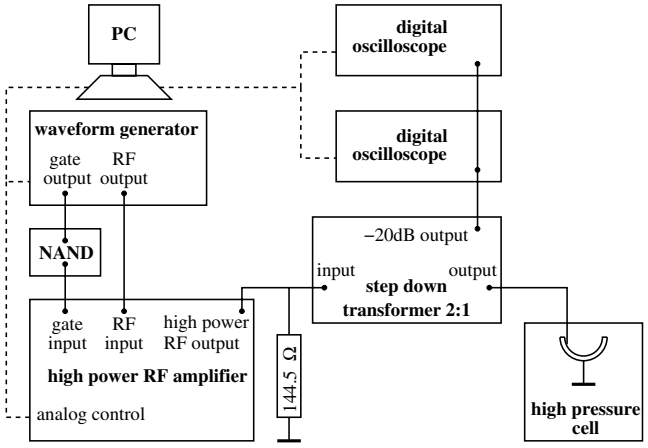

FIG. 3. Block diagram of the driving circuit of the transducer. The different units are designated in bold font. The solid lines represent the electrical connections, and the dashed lines the connections for computer control. The shunt resistor and the step-down transformer are used to improve the shape of the excitation voltage.

plotted the prediction of TWA. The lowest P_{cav} from Angell and his group [30] fall far away from other experiments, but close to the theoretical estimate. The discrepancy with other experiments cannot be accounted for by the difference in J; furthermore, two experiments (shock wave, and present work) have a higher value of J and give a less negative P_{cav}. One could think that the nature of the wall plays a role: water adhesion may be stronger on the quartz walls of the inclusions. However, we note that some acoustic experiments found $\simeq -20$ MPa in the absence of walls, and that Strube and Lauterborn [35], using the centrifugation method with quartz tubes, reached at best −17.5 MPa.

III. APPARATUS

To quench the liquid beyond the liquid-vapor equilibrium line, we use an acoustic method. We tried to improve on previous acoustic experiments (see Sec. II D) in the following ways. First, many of the acoustic experiments used rather long bursts, or even standing waves; this could enhance the sensitivity to minute quantities of dissolved gases because of a rectified diffusion process. Therefore we decided to use only short bursts. Furthermore, we wanted to decrease the parameter $V\tau$ (see Sec. I A), by using high frequency ultrasound; with a 1-MHz sound wave, we reach $V\tau \simeq 10^{-11}$ mm^3 s, even smaller than the inclusion work. The use of a small $V\tau$ reduces the effect of impurities and rules out the one of cosmic rays (their typical total flux at sea level is 240 m^{-2} s^{-1} [36]). We now present the experimental setup.

A. Generation and focusing of the acoustic pulses

Let us recall that some other acoustic experiments used parameters similar to ours [37–39]; but they failed to reach pressures negative enough to produce cavitation in clean water (see Sec. II D), and they had to add impurities on purpose. In order to reach more negative pressure, we chose a piezoelectric transducer with a hemispherical shape. This ensures a very narrow focusing of the sound wave (in an ellipsoidal region 3.5 mm^3 in volume, see Sec. IV C). Another advantage is that the negative pressure is developed in the bulk liquid, far away from any wall, which could trigger heterogeneous cavitation. These advantages were already used to study cavitation in liquid helium [40–42].

The transducer is a hemispherical shell, 16 mm inner diameter, 20 mm outer diameter, made of material P762 (Saint-Gobain Quartz), excited at resonance in its thickness mode at 1 MHz. Its impedance at resonance is real, equal to 26.5 Ω.

B. Choice of the driving voltage characteristics

The transducers are driven with a radio-frequency amplifier (Ritec Inc., GA 2500 RF). This amplifier is primarily designed to operate a 50-Ω resistive load. To match the transducer impedance, we use a high power downstep transformer and a resistor bridge. The best configuration found is shown in Fig. 3. We continuously monitor the voltage on the transducer side with a built-in −40-dB monitor on the transformer. A typical excitation signal at the cavitation threshold is shown in Fig. 4. We see that the voltage is nearly sinusoidal, although the envelope is not exactly rectangular; at the end of the pulse, there is also a small distortion followed by a slow relaxation of the voltage. To characterize the excitation, we chose to measure the root mean square voltage on the last undistorted cycle; we will refer to this quantity V_{rms} as the excitation voltage in the following.

Because the transducer is used at resonance, we need to choose correctly the center frequency f of the electric burst. All other parameters being fixed, we have studied the variation of the cavitation threshold (see Sec. IV B) with f and found a rather shallow minimum at 1025 kHz. We used this value for the mechanical resonance frequency throughout the study. It is close to the electrical one, and it is constant over the whole pressure and temperature range.

We need also to choose the burst length, on which V_{cav} depends because of the finite quality factor of the transducer: the longer the burst, the lower V_{cav}. However, there are two limitations: too short a burst makes V_{cav} beyond the reach of

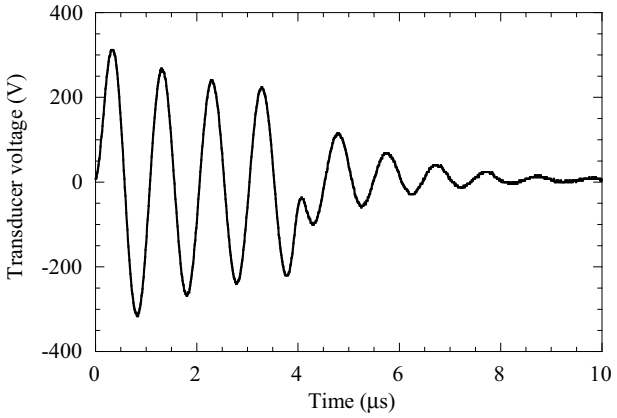

FIG. 4. Excitation voltage of the transducer, driven with a four-cycle burst, at the cavitation threshold at $T=20\ ^\circ\mathrm{C}$ and $P_{\mathrm{stat}}=1.7$ MPa. This corresponds to a peak power of 3.4 kW.

the amplifier (especially at high static pressure), and too long a burst makes the nucleation time distributed over several cycles, thus complicating the detection (see Sec. IV A). We found four to six cycle bursts to be a good compromise with a low enough required driving voltage, and a constant nucleation time (for given values of temperature and pressure). We have also checked that P_{cav} does not change when the burst length varies from 1 to 20 cycles.

C. Experimental cell

We have used two types of cells. Experiments requiring easy access to the focal region (e.g., calibration with a hydrophone, see Sec. IV C) were performed in simple Pyrex or stainless steel (SS) containers, open to the atmosphere. The second type of cell used was designed for high pressure operation (in particular for calibration by the static pressure method, see Sec. IV D). The corresponding setup is sketched in Fig. 5. The main body of the high pressure cell is a cylinder made of SS (5 mm thick). Its bottom is closed by a plate carrying the transducer and its holder. The seal is made with an indium wire. The tubing is made of SS (inner diameter 4 mm, outer diameter 6 mm). The connections are made by argon welding or using SS high pressure seals (Sagana). Other seals (at the pressure gauge, at the bellow, and between Pneurop fittings) are in bulk Teflon, to avoid pollution (see Sec. III E). A set of valves allows for pumping, filling, and pressure control. Before filling, the circuit is evacuated by pumping with an oil pump through a nitrogen trap or a dry scroll pump; water can then be transferred in the cell under vacuum. Once the system is filled with liquid, the valve near the cell is closed, and the pressure can be adjusted using a SS bellow, and monitored with a digital pressure gauge (Keller PAA-35S, range 0–30 MPa, accuracy ±0.015 MPa). The system is designed to sustain 24 MPa, but was operated below 10 MPa. The rest of the circuit, operated at low pressure, is connected with Pneurop fittings with Teflon O-rings. All the circuits were tested against leaks with a helium leak detector (Alcatel ASM 110 Turbo CL).

D. Temperature control

When a temperature control was needed, the cells were immersed in a bath. The open cells were immersed in a water

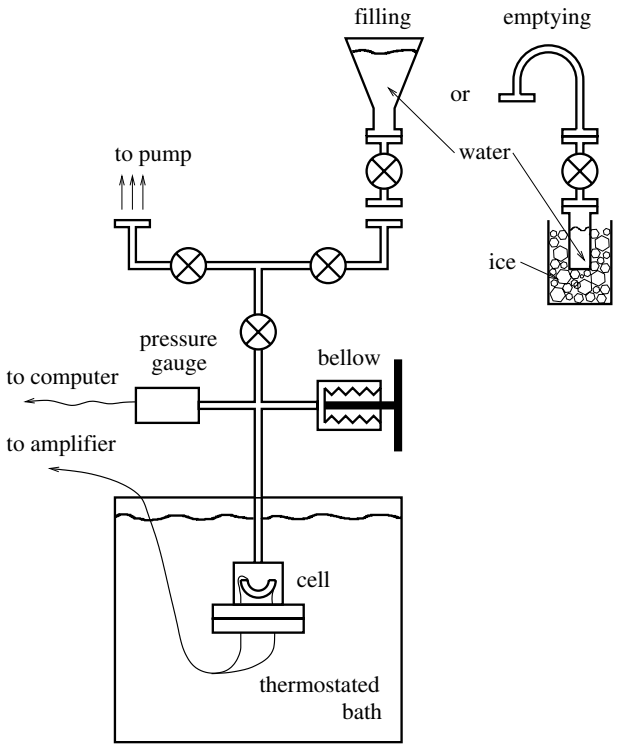

FIG. 5. Sketch of the experimental setup. The high pressure part contains the cell with the transducer, the pressure gauge, and the bellow for pressure control; it can be isolated from the rest by a valve. The use of two other valves allows evacuation (with an oil pump through a nitrogen trap or a dry scroll pump), filling (the flask with degassed water being connected), and emptying (the collecting vessel being connected and cooled with ice). The cell is immersed in a thermostated bath (operated between −10 and 80 °C). All the seals are made of SS or bulk Teflon, except the one at the bottom of the cell, which is made with an indium wire.

beaker on a heat plate (bath temperature regulated within 0.1 °C). The high pressure cell was immersed in a cryothermostat (Neslab RTE 300), regulating the temperature between −10 and 80 °C within 0.01 °C.

We refer to the temperature of the liquid away from the acoustic focus. One may wonder about the actual temperature inside the wave. Indeed, the liquid follows an adiabatic path, where the temperature is related to the pressure by

$$\left(\frac{\partial T}{\partial P}\right)_S = \frac{T V_{\mathrm{mol}} \alpha_P}{c_P}, \tag{4}$$

where V_{mol} and c_P are the molar volume and heat capacity at constant pressure, and α_P is the thermal expansion coefficient at constant pressure. When the liquid is stretched by the ultrasonic wave, it cools down or warms up, depending on the sign of α_P. To calculate the temperature change, one should integrate Eq. (4) over the appropriate pressure and temperature range. We will limit our discussion to an order of magnitude calculation. If we start from the LMD (4 °C at 0.1 MPa), where α_P is zero, there is no temperature change at low sound amplitude. To give numbers, let us use the tabulated data [43] at 50 °C and 0.1 MPa: $V_{\mathrm{mol}}=1.82\times10^{-5}$ m^3, $c_P=75.3$ J mol^{-1} K^{-1}, and $\alpha_P=4.4\times10^{-4}$ K^{-1},

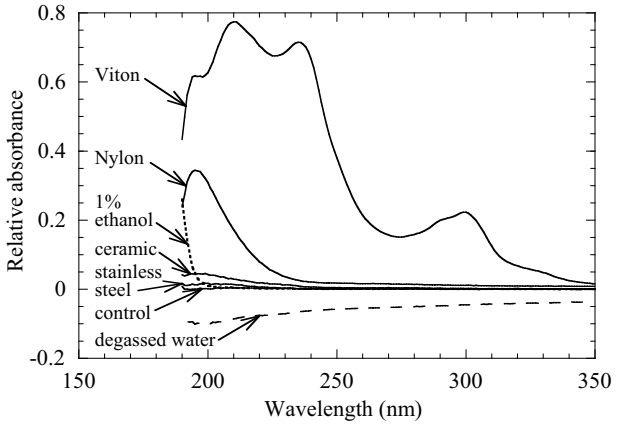

FIG. 6. UV absorption spectrum showing different "container effects." We used an automated spectrometer (Kontron Instruments, Uvikon 941) with quartz cuvettes (10 mm thickness). The reference cuvette was filled with ultrapure water directly drawn from the water polisher and sealed with a Teflon cap. The solid curves show the results of our test for several materials (designated by the labels), using the following procedure: a piece of the material was immersed in 50-mL ultrapure water in a Pyrex beaker, and the beaker was heated at 80 °C during 30 min, in contact with air. After cooling, water from this beaker was then used to rinse and fill the sample cuvette, and its UV absorption recorded. The control curve shows the results of this test for ultrapure water without adding any material. Other materials used in the cell (teflon tape, teflon tube, and indium wire, not shown) give absorption spectra between the control and that of stainless steel. For comparison, we also show the spectrum for a 1% ethanol solution in water (dotted line), and for ultrapure water degassed using the procedure described in Sec. III F (dashed line).

we find $(\partial T/\partial P)_S = 3.4 \times 10^{-8}$ K Pa^{-1}; with a negative swing of the wave of −20 MPa, we find a temperature change less than 0.7 K. We will neglect this effect and always refer to the bath temperature.

E. Materials

In order to reach homogeneous cavitation, special care must be taken in the preparation and handling of the water sample. For instance, dust particles or dissolved gases are expected to trigger cavitation at less negative pressures. Materials of the handling system and the sample cell were chosen in order to avoid the so-called "container effect" [44]. To do so, we checked the variation of the UV absorption of ultrapure water after being heated at 80 °C in contact with the material in an open Pyrex beaker. Typical checks are shown in Fig. 6. We kept the materials showing the smaller effect. The main materials involved were thus Pyrex glass and SS. Instead of the usual Viton O-rings, all seals (between Pneurop fittings, on the pressure gauge and on the bellow part) were made of bulk Teflon, except the bottom plate seal made of indium (see Sec. III C). The part of the pressure gauge in contact with the liquid is made of a SS membrane.

Let us describe in detail the materials used inside the high pressure cell. We used ceramic-SS electrical feedthroughs (CeramTec), argon welded to the cell bottom. A SS holder was designed to receive the transducer. Its two electrodes were connected mechanically to SS wires, to avoid using tin solder. The SS wire for the outer electrode is crimped on a SS sheet, and the assembly is pressed on the electrode by a screwable part of the holder; for the inner electrode we shaped a thin SS sheet into a spring to press onto the surface, and crimped it on the SS wire. We used 100-μm-thick Teflon to insulate this contact from the transducer holder. Finally the two wires were fitted in two Teflon tubes, and clamped to the feedthrough conductors by a SS tube with a SS screw on its side.

F. Water sample

The results reported here were obtained with ultrapure water drawn from a two stage water system (osmoser ELGA Purelab Prima, polisher ELGA Purelab Ultra) which achieves a resistivity of 18.2 MΩ cm and a total oxidizable organic carbon less than 2 ppb. However, it still contains dissolved gases, which are expected to lower the cavitation threshold. To degas the water, we used the following method: a 250 mL Pyrex glass erlenmeyer was modified to accept a Pyrex-SS fitting. It was cleaned with sulfochromic mixture, rinsed three times with ultrapure water, and filled with 100 mL of ultrapure water. The erlenmeyer was connected to a diaphragm pump (BOC Edwards D-Lab 10-8, vacuum limit 8 mbar, pumping rate for air 10 L min^{-1}) through a valve and a SS tubing, sealed with Teflon O-rings. After the end of the degassing, the valve is closed and water kept in contact with its vapor only; as the high pressure cell can be evacuated to a fraction of millibar, we can transfer the water sample into the cell without exposing water again to atmosphere.

The water was pumped continuously while being shaken in an ultrasonic bath (Transsonic T425/H). In principle, a better degassing is achieved at high temperature, because of the lower solubility of gases (around a factor of 1.6 less at 80 °C than at 20 °C); however, at high temperature, water evaporates with a high rate and condenses in the tubing and in the pump, thus reducing the pumping efficiency. Therefore we decided to keep the bath cold (20 °C), by circulating tap water inside a copper tubing. We observe the following behavior: at the beginning, many bubbles appear on the erlenmeyer walls; we attribute this to air degassing on cracks or weak spots in the glass. Then the bubbling slows down, and we can distinguish bubbles appearing in the bulk liquid, probably at a pressure antinode of the ultrasonic bath. Finally, the bubbling decreases gradually, and after 30 min, only large bubbles burst from time to time; we attribute this to boiling in a degassed sample. Our observations are similar to previous ones [25,27]. To check the water quality after degassing, we measured its UV absorption spectrum; Fig. 6 shows that UV absorption is even less than before degassing: we attribute this to the removal of dissolved oxygen, which absorbs UV light below 250 nm [45].

IV. OPERATION

We now turn to the measurements performed with our experimental setup. We first describe the methods of detec-

tion, then the statistics of cavitation, and finally our two ways of converting the excitation voltage into a negative pressure.

A. Detection of the cavitation bubbles

When the pressure becomes sufficiently negative at the focus, bubbles nucleate. In previous experiments on acoustic cavitation, bubbles were detected optically, by visual observation (directly or through a microscope) [25], high speed photography [46], light scattering [27], or even chemiluminescence [47,48]. They could also be detected acoustically, by the change in the pressure field used to produce cavitation [25] or by the sound emitted by cavitation (passive acoustic detection) [49]. Greenspan and Tschiegg [26] used the change in the quality factor of the resonator. Later on, Roy *et al.* [37] developed an active acoustic detection scheme: a high frequency sound wave is focused on the cavitation region, and backscattering is detected when bubbles are present; it is more sensitive than the passive detection method, leading to equal or less negative cavitation thresholds.

In the early stage of our experiment, we have investigated different detection methods in ethanol: light scattering, imaging on a charge-coupled device camera, passive acoustic detection, and the "echo method" [50]. All the methods were found to be consistent with each other, that is, to give simultaneously the same diagnosis about the presence or absence of a bubble. We will just describe here the echo method which we chose because of its simplicity to implement and its wide range of applicability. After the bubble is nucleated at the center of the hemisphere, the rest of the ultrasonic wave reaches the focal region, and part of it is reflected by the bubble surface, back to the hemispherical surface of the transducer. The reflected wave is converted back into a voltage, superimposed on the relaxation voltage of the transducer. Figure 7 shows a typical relaxation voltage with and without cavitation: the signals start to depart from each other at a time corresponding to the time at which the pressure burst reaches its minimum, plus the time of flight t_f of sound across the transducer radius $R=8$ mm: $t_f=R/c$, where c is the sound velocity.

One of the main features of the cavitation phenomenon we observe is its stochastic nature: if the acoustic bursts are simply repeated without changing any experimental parameter, we observe randomly echoes with or without cavitation. As the relaxation voltage in the absence of cavitation is very reproducible, it can be saved as a reference and subtracted from the following acquisitions. The cavitation events are then clearly detected from the low remaining electrical noise, for example by reading for each echo in a series the value of the peak-to-peak voltage. Figure 8 shows a typical histogram of the corresponding values over 1000 bursts: they fall into two well separated groups, which shows the reliability of this simple method.

Our echo method is evocative of the active detection method developed by Roy *et al.* [37]. To some extent, our method is simpler because it involves only one transducer for producing and detecting the bubbles, avoiding the need of a geometrical adjustment between the generator and detector used by Roy *et al.* [37].

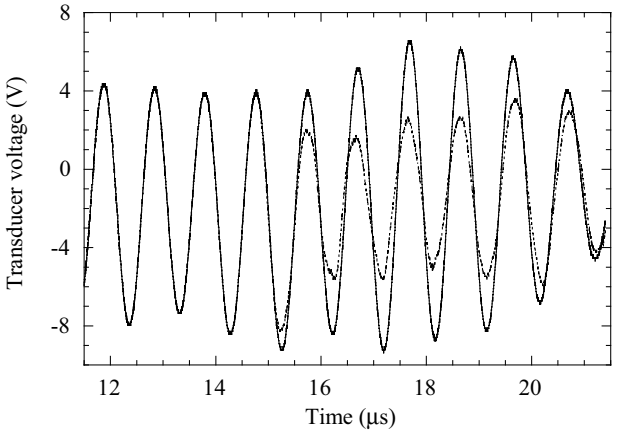

FIG. 7. Relaxation voltage of the transducer. The two traces were recorded for two successive four-cycle bursts with the same experimental conditions ($T=20$ °C, $P_{stat}=1.7$ MPa, $V_{cav}=163.3$ V). The solid line corresponds to the reproducible relaxation signal of the transducer coming back to rest, without cavitation. The dashed line is an example of the random echo signal reflected on the nucleated bubble and reaching the transducer voltage with a delay t_f after nucleation.

B. Statistics of cavitation

The randomness of the cavitation phenomenon leads us to define the cavitation probability Σ for a given set of parameters as the fraction of repeated bursts that exhibit cavitation, which is easily obtained from histograms such as the one shown in Fig. 8.

When the excitation voltage V_{rms} is increased, all other experimental parameters being held constant, Σ increases from 0 to 1 over a narrow range of V_{rms} values, as shown in

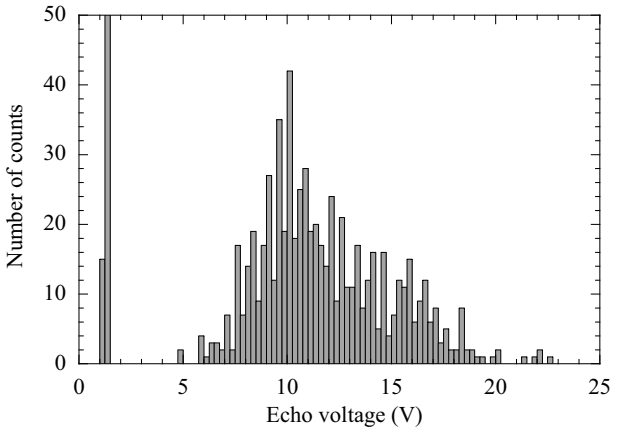

FIG. 8. Histogram of the peak-to-peak value of successive echoes. The left group of data shows the small noise on the excitation voltage without cavitation, the right one shows the various amplitudes reached by echoes with cavitation. The 1000 data points are distributed among 100 bins; the main peak (reaching 328 counts) is truncated for clarity.

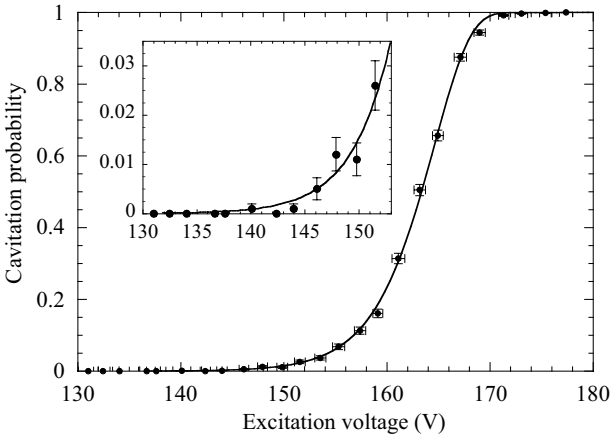

FIG. 9. Cavitation probability vs excitation voltage for four-cycle bursts at $T=20\ ^{\circ}\mathrm{C}$ and $P_{\mathrm{stat}}=1.7$ MPa. Each of the 25 data points was measured over 1000 repeated bursts. The standard deviation on the probability (calculated with the binomial law) is shown as error bars. The data are well fitted with Eq. (9) (solid line). The inset focuses on the low probability region, to show that zero probability is actually reached in the broad foot of the S curve.

Fig. 9. Because of their characteristic shape, we call these curves "S curves." Their steepness allows us to define accurately the cavitation threshold voltage V_{cav}, as the value of V_{rms} at which $\Sigma=1/2$.

We can investigate further the shape of the S curves. The energy barrier for cavitation depends on the negative pressure reached, which in turn depends on the excitation voltage V_{rms}. The cavitation rate (see Sec. I A) is related to these quantities by

$$\Gamma=\Gamma_0\exp\left(-\frac{E_{\mathrm{b}}[P(V_{\mathrm{rms}})]}{k_{\mathrm{B}}T}\right). \tag{5}$$

The cavitation probability writes $\Sigma=1-\exp(-\Gamma V\tau)$. The threshold V_{cav} (or equivalently P_{cav}) are reached when

$$E_{\mathrm{b}}[P(V_{\mathrm{rms}})]=k_{\mathrm{B}}T\ln\left(\frac{\Gamma_0 V\tau}{\ln 2}\right). \tag{6}$$

In the case of cavitation in a focused acoustic wave, the pressure varies in both space and time. By using an expansion around the minimum P_{min} of $P(\mathbf{r},t)$, one can calculate the effective $V\tau$; this was discussed in the case of cavitation in liquid helium [6], and gives for one cycle of a spherical sinusoidal wave:

$$V_{\mathrm{exp}}\tau_{\mathrm{exp}}=\frac{3^{3/2}\lambda^3\pi k^2T^2}{4\pi^2(\partial\ln E/\partial\ln|P|)^2E_{\mathrm{b}}(P_{\mathrm{min}})^2}. \tag{7}$$

Combining Eqs. (6) and (7), one obtains an implicit equation on P_{cav}. To solve it we need a theory for the energy barrier; for instance, if we use the prediction of the TWA, we find for water at 20 °C in a 1-MHz sound wave $P_{\mathrm{cav}}=-182.5$ MPa and

$$V_{\mathrm{exp}}\tau_{\mathrm{exp}}=\left(\frac{\lambda}{16.2}\right)^3\frac{\tau}{16.2}. \tag{8}$$

The values of $V\tau$ and P_{cav} do not depend much on the model used, because of the logarithmic derivative involved in Eq. (7).

The probability as a function of voltage involves a double exponential, so that it varies fast around the threshold; using a linear expansion of $E_{\mathrm{b}}[P(V_{\mathrm{rms}})]$ around V_{cav} in Eq. (5) will thus give a good approximation of Σ. This leads us to fit the experimental data shown in Fig. 9 with the following function:

$$\Sigma=1-\exp\left\{-\ln 2\exp\left[\xi\left(\frac{V_{\mathrm{rms}}}{V_{\mathrm{cav}}}-1\right)\right]\right\}, \tag{9}$$

where ξ and V_{cav} are free parameters. ξ measures the steepness of the probability curve, and is related to the energy barrier through

$$\xi=-\frac{V_{\mathrm{cav}}}{k_{\mathrm{B}}T}\left(\frac{\partial E_{\mathrm{b}}}{\partial V}\right)_{\Sigma=1/2}. \tag{10}$$

Figure 9 shows that the fit with Eq. (9) reproduces well the data, including the typical asymmetric shape (broad foot and narrow head). The quality of the fit is discussed in Appendix A. Zero probability is actually reached in the foot of the S curve; in one case we checked that, for V_{rms} in this region, no bubble was detected over 10 000 bursts. We measured the S curves to a high level of accuracy when we wanted to investigate in detail the cavitation statistics. When we were only interested in the value of the cavitation voltage, in order to gain time, we measured the probability over 300 or 400 bursts at four voltages around the threshold.

We would like to emphasize that this analysis is an improvement over the definition of the cavitation threshold used in the experiments done by other groups. Indeed, when the variation of probability with pressure was sufficiently sharp, the threshold was often arbitrarily estimated by the experimenter. Sometimes, it seems that only the most negative value observed for P_{cav} was reported; for instance, Strube and Lauterborn [35] used the centrifugation method and observed a large scatter of P_{cav} not detailed in the previous work by Briggs [21]. Only a few studies were concerned with statistics of the cavitation events [34,51]. The good repeatability of the acoustic pulses and the use of automated data acquisition allowed us to study these statistics with greater accuracy and more extensively.

One of the difficulties of our experiment lies in how to convert the excitation voltage of the transducer into a value of the negative pressure reached at the focus. One way is to rely on a calculation to convert the measured electrical power used by the transducer in acoustic energy [46]. To avoid the assumptions needed in this procedure, we prefer to use two independent methods of calibration that we shall now describe.

C. Pressure calibration with hydrophones

The first and most straightforward method uses calibrated hydrophones. They are needle shaped piezoelectric hydro-

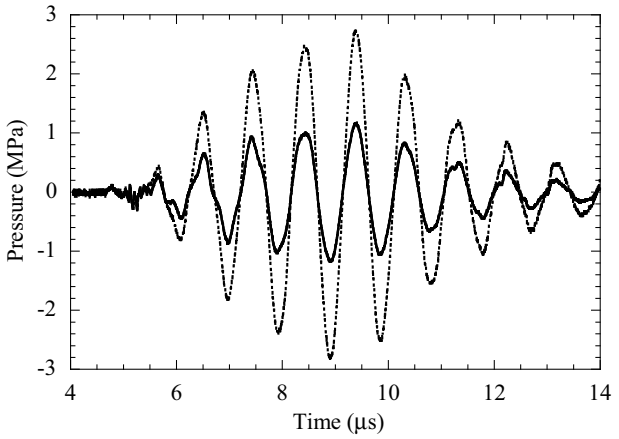

FIG. 10. Response of the 40-μm needle hydrophone at the focus. The hydrophone voltage has been converted into pressure using the manufacturer's calibration data. The solid (respectively, dotted) curve corresponds to an excitation voltage $V_{\mathrm{rms}}=7.21$ V (respectively, 17.42 V), that is 5.5% (respectively, 13.4%) of the cavitation voltage. The time scale starts with the excitation voltage, and the acoustic wave reaches the focus after the time of flight over the transducer radius ($t_f=R/c$, see Sec. IV A).

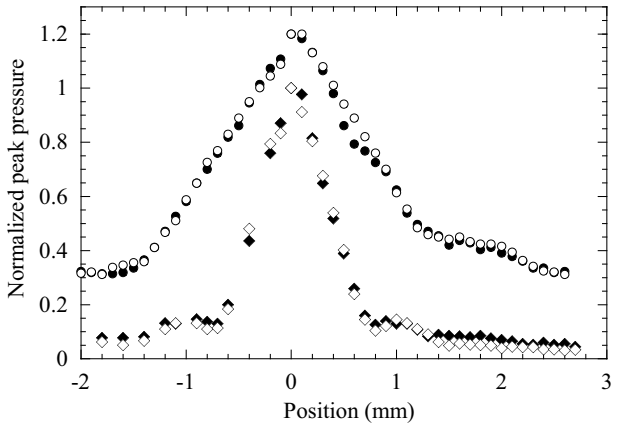

FIG. 11. Map of the acoustic field. The data (normalized to 1 at the focus) were taken with a 40-μm needle hydrophone in an open container at room temperature ($\simeq$25 °C), using one-cycle bursts. Filled (respectively, empty) symbols correspond to the maximum (respectively, minimum) pressure in a burst. Diamonds (bottom) show a scan in the equatorial plane of the transducer, whereas circles (shifted by 0.2 for clarity) show a scan along its axis.

phones (Precision Acoustics): the sensor is a disk made of a 9-μm-thick gold electroded Polyvinylidene difluoride (PVdF) film. We have chosen disk diameters of 40 and 200 μm at the end of needles 300 and 460 μm in diameter, respectively. The probe is very fragile, and cavitation on its surface causes irreversible damages. We have thus performed the calibration of the ceramic transducer with ultrapure degassed water; as the calibration had to be done in an open tank, we worked only a few hours with the same water sample. To avoid cavitation, we also had to use excitation voltages significantly lower than the cavitation threshold. To determine this threshold, S curves were measured immediately before and after the use of the hydrophone; to avoid damage, the hydrophone was removed from water while acquiring the S curves. We noticed a small drift in the cavitation voltage, attributed to the change in water conductivity because of its exposure to air; indeed, the transducer electrodes are in contact with water and an increase in its conductivity decreases the efficiency of the transducer for a given excitation voltage. However, this shift was less than 1.5% over the time needed for the calibration with one needle.

The needle hydrophone is inserted along the axis of the hemisphere. To find the position of the focus, we repeat a given low amplitude acoustic burst and we look for the position which maximizes the peak-to-peak voltage of the hydrophone response. This can be done with an accuracy of around one quarter of the sensor diameter, using micrometer screws. A typical signal thus obtained is shown in Fig. 10. The manufacturer provides calibration data for the complete hydrophone system, every 1 MHz from 1 to 20 MHz, with a stated uncertainty on the gain of 14%. We have converted the voltage given by the hydrophone into pressure using both a direct conversion with the gain tabulated at 1 MHz, and a deconvolution technique using the gain at all frequencies: because the wave has a small harmonic content (see Fig. 10), the two techniques give no noticeable difference.

We have performed a detailed mapping of the acoustic field. The results are shown in Fig. 11. One can see that the focusing is sharp, with an ellipsoidal shape, 1.5 mm (one wavelength λ) across and $\simeq$3 mm ($\simeq 2\lambda$) along the transducer symmetry axis; for a complete sphere, one would expect a spherical focus of diameter λ. From the known variation of the sound velocity [43], we calculate that the focal volume changes by less than 20% over the range of temperature and pressure used in the experiment.

We recorded the hydrophone signals for different values of the excitation voltage of the transducer, typically up to 1/5 of the cavitation threshold, because distortions sometimes appeared at this level. They could be due either to heterogeneous cavitation on the hydrophone, or to nonlinearity of the hydrophone response at this large amplitude (although the manufacturer gives a pressure range of use exceeding 20 MPa rms). In one case, we went up to 14 MPa, but afterwards the hydrophone appeared to be broken. Figure 12 shows a set of results for the same transducer and water sample: the different hydrophones used give results consistent with each other. The relation between the peak pressure at the focus and the excitation voltage is found to be linear, within the experimental error. If we extrapolate up to the cavitation voltage, we obtain at 25 °C: $P_{\mathrm{min}}=-21$ MPa (respectively, $P_{\mathrm{min}}=-24.5$ MPa) for the 40 μm (respectively, 200 μm) needle. The manufacturer gives a calibration uncertainty on the gain of 14%, which means that the results from the two needles are consistent with each other.

One may wonder if the presence of the hydrophone affects the pressure field. This seems unlikely because of its needle shape which allows to handle it from a direction that the acoustic wave reaches only after the focus. Building up of a stationary wave is not expected, because the size of the sensor tip is smaller than the sound wavelength (1.5 mm), and because the acoustic impedance of PVdF is close to the one of water. Furthermore, the two different sized hydro-

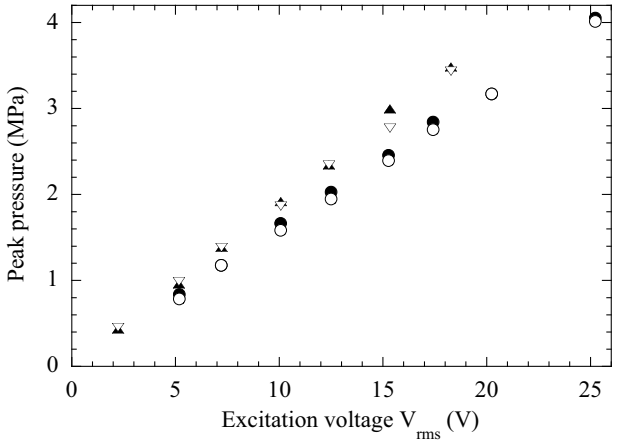

FIG. 12. Peak pressures measured by the hydrophones as a function of the transducer excitation voltage. The data were taken in an open container at room temperature ($\simeq$25 °C, with four-cycle bursts, the cavitation threshold voltage being V_{cav}=130 V). Filled (respectively, empty) symbols correspond to the maximum (respectively, minimum) pressure in a burst. Circles (respectively, triangles) were obtained with a 40-μm (respectively, 200 μm) needle. The manufacturer gives a calibration uncertainty on the gain of 14%, which means that the results from the two needles are consistent with each other.

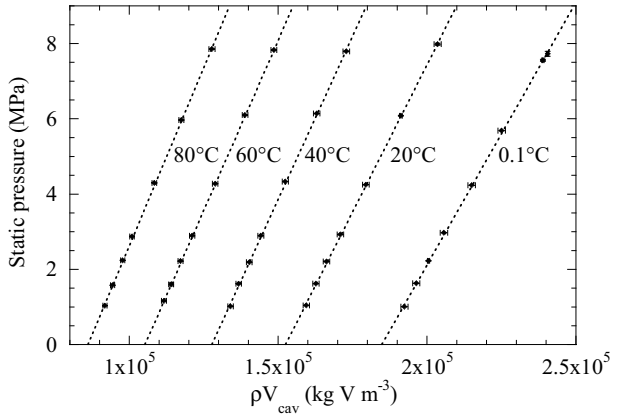

FIG. 13. Static pressure as a function of the product ρV_{cav} for 5 of the 15 temperatures investigated in run 0. The dotted lines are linear fits to the data; each set is labeled (on the right) with the temperature. Experimental error bars are shown on each data point; most of the vertical errors are too small to be seen at this scale.

phones lead to the same results, given further support for our method.

The hydrophone signals have the shape of a modulated sine wave and do not show any sign of shocks. But for the larger pressure amplitudes involved to reach cavitation, one may wonder about the linearity of the focusing, which we assume when extrapolating the hydrophone measurements. In fact, because the sound velocity is an increasing function of pressure, one expects that nonlinearities will develop in the following way: the pressure at the focus should deviate from a symmetric sine wave when the amplitude increases, exhibiting shallow and wide negative swings and narrow and high positive peaks, with the possibility of shock formation. This behavior is observed in numerical simulations of the spherical focusing of a wave in liquid helium, and confirmed experimentally [52]. However, these nonlinearities are not noticeable if the pressure amplitude is small compared to the spinodal pressure, which seems to be the case in our experiment (−26 MPa compared to −200 MPa, according to Speedy EOS). Furthermore, we think that the nonlinearities are much less pronounced in the hemispherical geometry, presumably because the velocity at the focus is not required to vanish, whereas it is for the spherical geometry [52,53]. Anyhow, even if nonlinearities were present, they would lead to a less efficient buildup of the negative swing at large amplitudes, so that the linear extrapolation of the hydrophone measurements gives a lower bound for P_{cav}.

D. Calibration by the static pressure method

The second method of calibration we use is based on the application of a static overpressure to the liquid. It is similar to the method used by Briggs *et al.* [54] and Greenspan and Tschiegg [26], and also in our group to study cavitation in liquid helium [41,42]. The range of overpressure explored in the present study is more than tenfold that of the previous ones. We produce this overpressure with the bellow described in Sec. III C; we will refer to it as the "static" pressure P_{stat} to distinguish it from the acoustic pressure. When starting from a higher P_{stat}, to reach the same value of P_{cav} at the focus, one has to use a higher excitation voltage. It can be shown [52] that if the focusing is linear, the pressure swing in the wave $\Delta P = P_{stat} - P_{min}$ is proportional to $\rho(P_{stat})V_{rms}$, where $\rho(P_{stat})$ is the density of the liquid at rest; the marginal variation of ρ with pressure and temperature was taken into account in our analysis. Therefore the data P_{stat} vs $\rho(P_{stat})V_{cav}$ should fall on a line crossing the axis V_{cav}=0 at the pressure P_{cav}. Taking the nonlinearities into account, the intercept thus obtained should give an upper bound for P_{cav} [52]. The results of the static pressure method will be presented in Sec. V A. As we shall see, its result at room temperature agrees well with the hydrophone calibration. At other temperatures, we use only the static pressure method.

V. RESULTS

A. Pressure dependence of the cavitation voltage

Let us now discuss the pressure dependence of the cavitation voltage at a given temperature. We begin with the results at high pressure. We give the example of the first run (later referred to as run 0), where the number of temperatures investigated (15) was larger than in subsequent runs. Figure 13 shows typical results for P_{stat} as a function of the product $\rho(P_{stat})V_{cav}$. For each temperature, the data above 1 MPa fall on a straight line. In one of the following runs, we even pressurized the sample cell up to 20 MPa: the corresponding data point fell on the extrapolation of the straight line obtained by fitting the data between 1 and 9 MPa. This linear behavior supports the validity of the static pressure method (see Sec. IV D), and shows that nonlinearities are weak. The

pressure extrapolated to zero voltage will be taken as the cavitation pressure; its variation with temperature will be presented in Sec. V B.

The error bars in Fig. 13 come from the noise on V_{rms} (at a given level, the standard deviation is less than 1% of the average), and from the less relevant fluctuations in pressure (due to the part of the high pressure setup that stands out of the thermostated bath, see Fig. 5). From the linear relation between P_{stat} and ρV_{cav}, we have estimated the uncertainty on P_{cav} [55]. For run 0, we find between ±0.3 MPa and ±0.8 MPa (see Sec. V B).

We can compare the results of both calibrations at 25 °C. The static pressure method gives −23.6±0.5 MPa, whereas the 40 μm (respectively, 200 μm) needle hydrophone gives P_{min}=−21±2.9 MPa (respectively, P_{min}=−24.5±3.4 MPa) (the uncertainty comes from the 14% uncertainty on each hydrophone gain). These values are remarkably close, which supports our whole calibration procedure. Because they shall give respectively a lower and an upper bound of P_{cav}, their vicinity also confirms that nonlinearities are negligible.

To be exhaustive, we have to mention two problems encountered in our study: a hysteretical behavior observed just after filling the experimental cell, and an anomaly in the variation of V_{cav} at low pressures.

Before filling, the cell is put under vacuum. It is cooled to 4 °C and then connected to the degassed water sample at saturated vapor pressure and room temperature. Water flows inside the cell. After a few minutes, the isolation valve is closed, and the pressure in the cell can be varied with the bellow. During the first pressurization, we increased the pressure step by step beween 0 and 9 MPa, measuring at each step the cavitation voltage. We noticed that the curve obtained during the first pressurization always differed from the following curves. Furthermore, the S curves (see Sec. IV B) of this first pressurization were noisy or even hysteretical, and the histograms of the echo signal did not exhibit a clear threshold; these anomalies occurred only for the first (low pressure) points of the first pressurization. On the other hand, if water was kept at 9 MPa for some time (typically half an hour), the following S curves and histograms (at all pressures) were satisfactory, and the curves $P_{stat}(\rho V_{cav})$ obtained by depressurizing or pressurizing the liquid fell on top of each other without hysteresis. These results are summarized in Fig. 14.

Another, more persistent anomaly was detected: at low pressure, an elbow appears in the curves $P_{stat}(\rho V_{cav})$, slightly more pronounced at lower temperature. We have checked that the elbow was still present after pressure cycles (increasing P_{stat} from 0 to 9 MPa, keeping the system at 9 MPa for 2 h, and then repeating the measurements when decreasing P_{stat} back to 0); the cavitation voltages in the elbow were reproducible and did not show any hysteresis. This means that the source of the elbow (or more precisely its effect on cavitation) disappears above 1 MPa, and reappears below this value.

We see two possible reasons for this behavior. (i) Either cavitation nuclei are present, and give a cavitation threshold which itself depends on the cavitation pressure, causing the failure of the static pressure method. Just after filling, they would be of larger size than after the first pressure cycle, thus

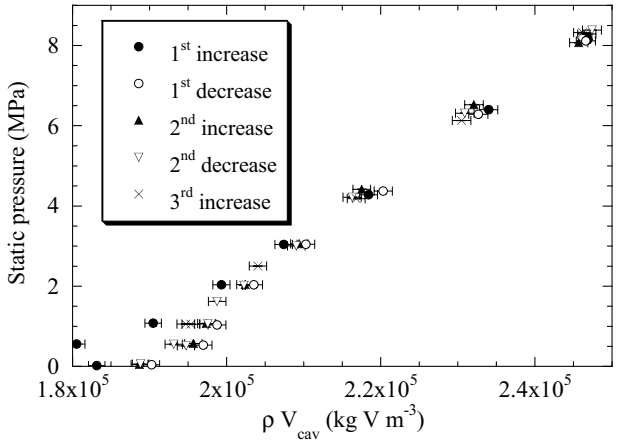

FIG. 14. Static pressure as a function of the product ρV_{cav} during the first pressure cycles of run 3 at 0.1 °C.

explaining the observed hysteresis. These nuclei could be undissolved gas bubbles (possibly entrapped on solid particles). By Laplace's law, for such trapped bubbles not to dissolve at 20 MPa (the highest pressure reached in one run), the interface with the liquid should reach a radius of curvature of 7 nm. It seems unlikely that impurities with the correct geometry and wetting properties could exist in sufficient concentration to explain our results. Morevover, we shall see in Sec. V C that the statistics of cavitation are the same at all static pressures. (ii) Or the properties of the transducer itself are pressure dependent, leading to an artifact in the pressure dependence of the cavitation voltage. As the mechanical resonance frequency was measured to be pressure independent (see Sec. III B), we must look for another source of artifact. One can find appropriate sites for bubble trapping inside the transducer itself. The piezoelectric material is porous, made of ceramic grains around 10 μm, and, whereas the electrodes are not permeable to water, the edge of the transducer is not, and is able to let the liquid enter the pores, thus changing the efficiency of the transducer (e.g., by modifying its dissipation and quality factor). Just before filling, the transducer is completely dry. When P_{stat} increases from 0 to 1 MPa (corresponding to a meniscus with a radius of curvature of 140 nm), water would invade most of the pores volume, giving a measurable effect on V_{cav}. A further increase of P_{stat} would only affect the remaining free volume (filled with vapor), without a noticeable change of the transducer efficiency; but some sites with bottlenecks less than 7 nm would keep some vapor even at 20 MPa, allowing the vapor phase to grow again inside the pores, thus explaining the absence of hysteresis during the following pressure cycles.

Despite the two anomalies just described, we are confident in the use of the static pressure method at high pressure, which is supported by the hydrophone calibration, and the good reproducibility of results (see Sec. V D). In our data analysis, we decided to keep only the high pressure part of the curves $P_{stat}(\rho V_{cav})$ (that is for 1 MPa$\leqslant P_{stat} \leqslant$9 MPa, as in Fig. 13).

B. Temperature dependence of the cavitation pressure

Figure 15 displays P_{cav} in run 0 (obtained as described in Sec. V A) as a function of temperature. We can compare this

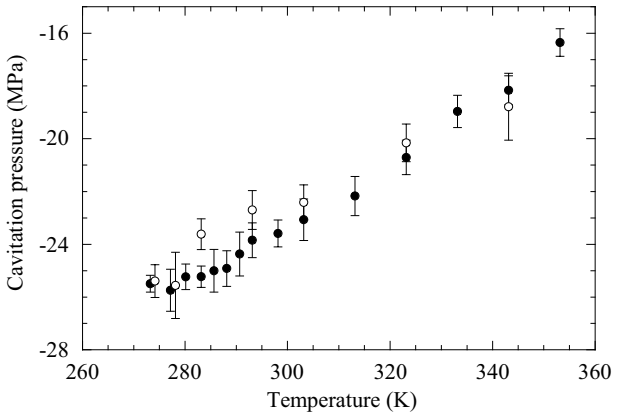

FIG. 15. Cavitation pressure as a function of temperature. P_{cav} was obtained with the static pressure method (see Sec. IV D). Run 0 (filled circles) is compared to our preliminary results (Ref. [56]) (empty circles). The uncertainties on P_{cav} were calculated as described in Sec. V A.

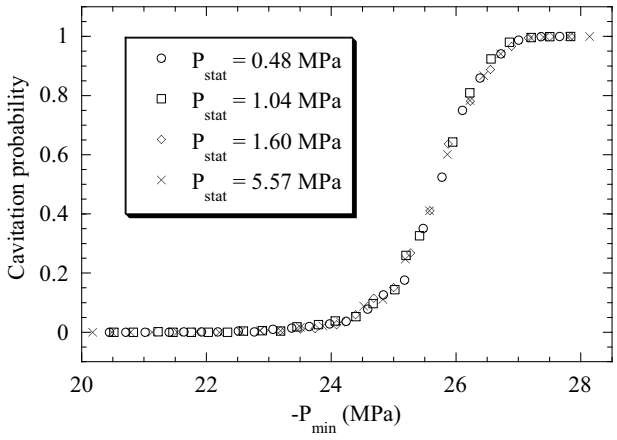

FIG. 16. Cavitation probability as a function of the minimum pressure reached in the wave for four different static pressures. Each point is an average over 1000 bursts. The data were taken during run 0 at $T=4$ °C.

work to our preliminary results [56]. At that time, we used another hemispherical transducer, resonating at 1.3 MHz. P_{cav} was also obtained with the static pressure method, but P_{stat} varied only between 0 and 3 MPa, and the problem of the low pressure elbow (see Sec. V A) was not yet noticed. Keeping in mind these differences, the agreement with the present work is satisfactory.

We find a monotonous temperature variation, with P_{cav} becoming less negative as T is increased: it varies from −26.4 MPa at 0.1 °C to −16.5 MPa at 80 °C. There is no obvious minimum, or if a minimum exists it is very shallow. Anyhow, the experimental results disagree with both theories as regards the magnitude of P_{cav} ($\simeq -24$ instead of −120 MPa). We will come back to this in Sec. VI.

Let us add a special comment concerning the low temperature part. Because of the negative slope of the melting line of water in the P-T plane, stretched water at low temperature is metastable against vapor *and* ice formation: this is called the *doubly metastable region*. Henderson and Speedy [18] have reported the largest penetration in this region: from −19.5 MPa at 0 °C to −8 MPa at −18 °C. The present study exceeds these values, with −26 MPa at 0.1 °C. We have also observed cavitation at −0.6 °C, but as we kept $P_{stat}=8.5$ MPa to avoid bulk freezing, we could not calibrate the pressure by the static pressure method.

Before discussing the discrepancy between theory and this experiment, we will report on how we have checked its reproducibility.

C. Statistics of cavitation

The results reported in Secs. V A and V B involved only the measurement of the cavitation voltage. Relatively short acquisitions of S curves (typically four values of the excitation voltage each corresponding to 400 repeated bursts) are sufficient for this purpose. We have also investigated the steepness ξ of the S curves [see Sec. IV B, Eq. (9)]. To get enough accuracy on ξ, one needs much longer acquisitions: we used typically 25 values of the excitation voltage each corresponding to 1000 bursts; details about the accuracy of the S-curve parameters are given in Sec. A. At $f_{rep}=1.75$ Hz, this corresponds to 4 h, during which the experimental conditions must remain stable. The temperature stability of the experimental region is excellent, controlled by the thermostated bath. The pressure is more subject to fluctuations, because of the temperature change of the emersed part of the handling system. We recorded the pressure and found it to be always stable within a few percent.

The validity of the static pressure method shows that P_{cav} is independent of P_{stat}. We can thus convert the excitation voltage V_{rms} used at any static pressure P_{stat} into the minimum pressure P_{min} reached in the wave:

$$P_{min} = P_{stat} + (P_{cav} - P_{stat})\frac{V_{rms}}{V_{cav}}, \tag{11}$$

where V_{cav} is determined by fitting the S curve with Eq. (9). The S curves can now be plotted with the cavitation probability vs P_{min}, and fitted with

$$\Sigma(P_{min}) = 1 - \exp\left\{-\ln 2 \exp\left[\xi\left(\frac{P_{min}}{P_{cav}} - 1\right)\right]\right\}. \tag{12}$$

Similar to Eq. (10), ξ is related to the energy barrier for cavitation through

$$\xi = -\frac{P_{cav}}{k_B T}\left(\frac{\partial E_b}{\partial P}\right)_{P_{cav}}. \tag{13}$$

The estimation of the uncertainty on the fitting parameters is discussed in Appendix A.

In run 0, we have measured accurate S curves at 4 °C and several values of P_{stat}. They are compared in Fig. 16: the agreement is excellent. The values of ξ and the quality of the fits are compared in Table II. The value of P_{cav} is the same by construction, but the fact that the steepness of the curves is constant shows that the statistics of cavitation is not affected by the application of a static pressure. Interestingly, this conclusion holds at $P_{stat}=0.48$ MPa, in the elbow mentioned in Sec. V A: this rules out the possibility that cavita-

TABLE II. Results of the fit with Eq. (12) for the S curves of Fig. 16. P_{stat} is measured for each burst, and then averaged for the 1000 bursts with the same excitation voltage. To illustrate the stability of P_{stat} during the acquisition of an S curve, we give for each curve the average and the extreme values of this set of P_{stat}.

P_{stat} (MPa)				
average	min.	max.	ξ	χ^2
0.48	0.45	0.51	45.2±1.3	3.6
1.04	1.01	1.06	44.7±1.1	2.6
1.60	1.58	1.62	44.0±1.8	6.6
5.57	5.56	5.58	43.3±1.2	3.1

tion nuclei are responsible for this elbow. We have also studied the temperature dependence of ξ, measured at P_{stat} = 1.6 MPa. The result is shown in Fig. 17. The value predicted by TWA is

$$\xi_{TWA} = 2 \ln\left(\frac{\Gamma_0 V \tau}{\ln 2}\right). \quad (14)$$

Using the values from Eqs. (2) and (8) (with R_c=1 nm), one gets $\xi_{TWA} \simeq 95$, practically independent of temperature in the range of interest. We have checked that this value can not be reduced to the measured ones by the experimental noise (see Appendix A). We will come back to this discrepancy in Sec. VI.

D. Reproducibility of results

To check the reproducibility of the results, we have repeated the measurements using the same procedure for a series of eight runs, restricting the study to four values of the temperature (0.1, 20, 40, and 80 °C), and at each temperature five values of the pressure (around 1.1, 2.5, 4, 6, and 8 MPa). Between each run, the cell was dried and evacuated in the following way. First, most of the water was transferred by evaporation-condensation from the cell heated at 80 °C to a container cooled at 0 °C, without contact with the atmosphere (see Sec. III C, Fig. 5). A dry diaphragm pump was then used to evaporate the remaining liquid, and finally the cell was pumped through a nitrogen trap by an oil pump to achieve a good vacuum. Alternatively, we could use a dry scroll pump for the last two steps. The system was ready to be filled again with water degassed as explained in Sec. III F in order to start a new run.

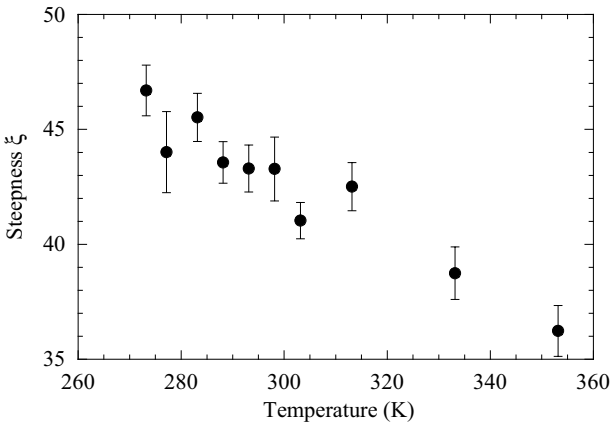

FIG. 17. Steepness of the S curves as a function of temperature. Data were measured in run 0, using 25 points with statistics over 1000 bursts, at P_{stat}=1.6 MPa.

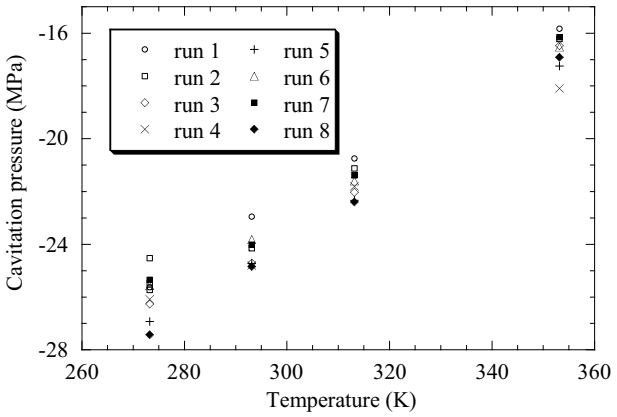

FIG. 18. Cavitation pressure as a function of temperature, obtained with the static pressure method (see Sec. IV D), for runs 1–8. The error bars are omitted for clarity; they are similar to those in Fig. 15.

The curves $P_{cav}(T)$ obtained for the eight runs are shown in Fig. 18. At each temperature, values of P_{cav} fall in a ±1 MPa pressure range, except at 0.1 °C where the scatter reaches ±1.7 MPa. This is only slightly larger than the uncertainty on P_{cav} that we expect from the static pressure method, between ±0.3 MPa and ±0.8 MPa (see Sec. V A). The average value of P_{cav} varies from −26 MPa at 0.1 °C to −17 MPa at 80 °C.

We have also considered the reproducibility of results during the same run. As explained above, except for the very first pressurization after filling, the curves $P_{stat}(\rho V_{cav})$ showed no hysteresis. For some of the runs and temperatures, we have repeated the measurement of P_{cav} by the static pressure method after a time interval which could reach nine days. For some of the eight runs, we observed a small drift in the value of V_{cav} at a given P_{stat} (less than 1%). However, the value of P_{cav} was always found to be stable within ±0.2 MPa, except at 0.1 °C where the variation could reach ±0.75 MPa.

After each run, the UV absorption spectrum of the water collected by evaporation-condensation was recorded. As can be seen in Fig. 19, each spectrum shows a similar increase of absorption (compared to ultrapure water) in the range 190–240 nm. If one compares with the spectra obtained in ultrapure after contact with each material in the cell (Sec. III E, Fig. 6), we may attribute this increase to the ceramic material of the transducer.

VI. DISCUSSION

The experimental method used in this study gives more negative values for the cavitation pressure than others, except the one using mineral inclusions (see Sec. II). In our

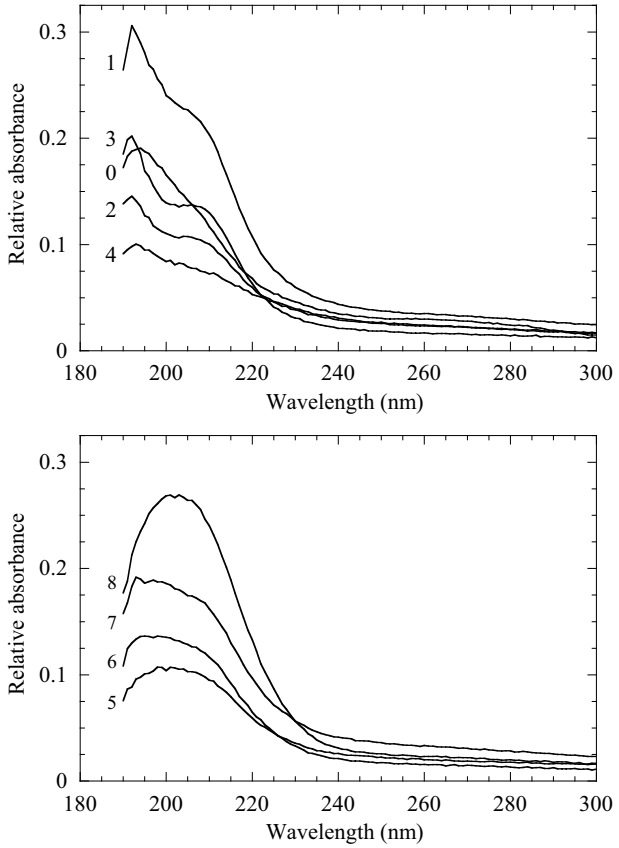

FIG. 19. UV absorption spectrum of the water collected from the experimental cell for nine successive runs. We used an automated spectrometer (Kontron Instruments, Uvikon 941) with quartz cuvettes (10 mm thickness). The reference cuvette was filled with ultrapure water directly drawn from the water polisher and sealed with a Teflon cap. The label indicates the run number.

case, the pressure was calibrated by two independent methods in good agreement with each other. In addition, the acoustic technique allows a detailed investigation of the cavitation statistics and a clear definition of the cavitation threshold. The results are highly reproducible, in contrast with other studies in which cavitation pressures can be highly scattered and time dependent, and sometimes only their most negative values are reported. This is made possible because in our experiment, the negative pressure is developed during a short time, in a small experimental volume far from any wall: the influence of impurities, if any, is greatly suppressed.

However, despite these advantages, we have not reached the highly negative cavitation pressures observed in the inclusion work. In fact, there is a large gap in cavitation pressure data between the inclusion work (reaching $P_{cav} < -100$ MPa at room temperature) and *all* other experiments ($P_{cav} > -30$ MPa) (see Sec. II F). We can attribute the discrepancy between the present work and the inclusion work to three possible reasons: (i) impurities; (ii) error in the pressure estimate in the inclusion work; and (iii) error in the pressure calibration of our experiment. We can rule out reason (iii), because of the good agreement we find between two independent calibration methods (see Secs. IV C and IV D). We also emphasize that our values of the cavitation pressure are close to those reported in experiments were a direct measurement of the pressure was available (from the centrifugal force [21] or with pressure gauges [17–19]). Let us examine the two other hypotheses and their implications.

In Sec. VI A, we present some models of heterogeneous cavitation, and compare their predictions for the statistics of cavitation with our measurements. We have also investigated different water samples, with different preparation or origin, in order to vary their possible content in impurities; the results are presented in Sec. VI B. Finally, we discuss the pressure calibration in the inclusion work in Sec. VI C.

A. Impurities and cavitation statistics

In this section we will discuss the possible effect of impurities on the statistics of cavitation. In particular, we are interested in the information that can be obtained from the accurate measurements of the cavitation probability vs excitation voltage (S curve) presented in Sec. IV B.

We can think of different kinds of impurities. First we consider impurities which lower the energy barrier for cavitation $E_b(P)$; let us call them type-I impurities. These could be surfactant molecules, reducing the energy cost associated with the creation of a liquid-vapor interface, or dissolved molecules that change the local structure of water (e.g., by disrupting the network of hydrogen bonds). For example, the observed cavitation pressure could be explained within the TWA model [Eq. (3)] if the surface tension σ is changed to an effective value: for instance, $\sigma_{eff}=18.7$ mN m^{-1}, would give $P_{cav}=-24$ MPa at 20 °C.

For simplicity we suppose that we have only one kind of type-I impurities, that is, they all lead to the same modified energy barrier. If their concentration n_0 is sufficiently high [typically $n_0(\lambda/16)^3 \gg 1$, see Eq. (8)], the cavitation probability for a minimum pressure P_{min} in the wave will be given by Eq. (12) as for homogeneous cavitation, except that the cavitation pressure P_{cav} will be lowered. We already know (see Fig. 9) that this model provides a good description of the data. The distribution of impurities can be more complicated: for instance, for surfactant molecules at a concentration below the critical micellar concentration, the size distribution of micellar aggregates is a decreasing function of size [57]. If E_b reaches a minimum at an optimum aggregate size, the relevant concentration would then be the total concentration of impurities with E_b within a small interval ($\simeq k_B T$) around this minimum.

Now we consider a different kind of impurity, with a deterministic effect on cavitation; let us call them type-II impurities. We assume that to each impurity is associated a threshold pressure $P_t < P_{sat}$, and that cavitation will occur if and only if the impurity is submitted to a pressure more negative than P_t. Type-II impurities could be vapor bubbles, either stabilized by an organic shell [58], or pinned in a crevice on a hydrophobic particle and stabilized by their radius of curvature [59,60]. The typical radius R of such bubbles can be estimated with Laplace's law: $R=2\sigma/P_t$; for $P_t \simeq -25$ MPa and using for σ the bulk surface tension of water, one finds $R \simeq 5.8$ nm.

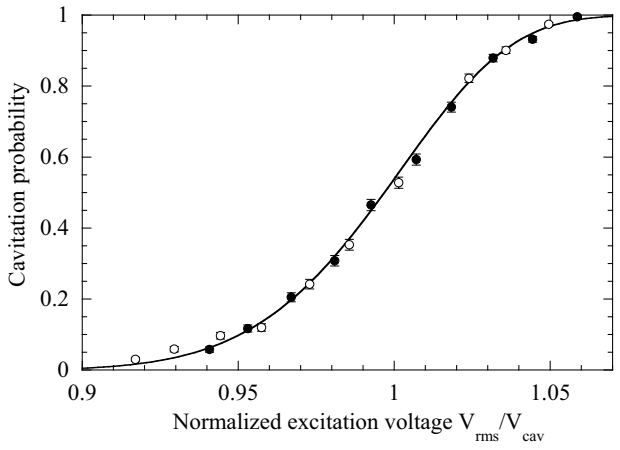

FIG. 20. Cavitation probability as a function of the excitation voltage normalized by the cavitation voltage. Each filled (respectively, empty) circle shows the probability measured with a 1 -MHz (respectively, 1.3-MHz) transducer, by counting the cavitation events over 1000 bursts, at room temperature in an open Pyrex container. A fit with Eq. (B8) (solid line), using $P_2/P_{cav}=0.8$ and $\alpha=11/2$, gives $n_0\lambda^3[P_{cav}/(P_2-P_1)]^{13/2}=(3.62\pm0.10)10^7$ for both frequencies.

The statistics of cavitation will depend on the distribution of type-II impurities. We have investigated several distributions (the calculations are given in Appendix B). We have found that a fifth-power-law distribution between pressures P_1 and P_2 (see Appendix B, inset of Fig. 25) provides a good fit; it could still be improved by changing the distribution. The fitting procedure leads to the total concentration of impurities n_0 through $n_0\lambda^3/(P_2-P_1)^6=41.4$ MPa^{-6}. P_2-P_1 must be larger than the width of the probability curve, $\simeq 5$ MPa; this leads to a lower bound on the concentration: $n_0 \geqslant 1600$ mm^{-3}.

Is it possible to distinguish between type-I and type-II impurities? The strongest difference between both kinds of impurities is the dependence with the frequency of the sound wave. On one hand, for type-I impurities, a change in the frequency will affect V and τ [see Eq. (7)], but only slightly P_{cav} and ξ because of the logarithm in Eq. (6). On the other hand, the S curve for type-II impurities involves $n_0\lambda^3$ (see Appendix B). In our preliminary study we used a transducer resonating at 1.3 MHz instead of the transducer at 1 MHz; between these two frequencies the value of λ^3 changes by a factor of 2.2. We have already seen that the respective cavitation pressures were very close (see Fig. 15). If we compare accurate S curves measured for each frequency under the same experimental conditions, we find that the slopes are equal. However, one can argue that as each transducer was used with a different water sample, this may be a coincidence. To rule this out, we have repeated the measurement of accurate S curves for a 1-MHz and a 1.3-MHz transducer immersed in the *same* ultrapure water sample in an open Pyrex container. Figure 20 shows that the slope is the same. We have normalized the excitation voltage by the cavitation voltage, assuming the cavitation pressure to be the same for both transducers as found before. Using Eq. (B8) with $P_2/P_{cav}=0.8$, the best fit is obtained with a 11/2 power law, and gives $n_0\lambda^3[P_{cav}/(P_2-P_1)]^{13/2}=(3.62\pm0.10)10^7$ [respectively, $(3.62\pm0.12)10^7$] for the 1-MHz (respectively, 1.3 MHz) transducer. In the case of cavitation on type-II impurities, this parameter would change by a factor 2.2, which is large enough to be detected by our accurate cavitation statistics. We can therefore exclude the possibility that cavitation is heterogeneous on type-II impurities.

We have only considered type-I impurities in large concentration $[n_0(\lambda/16)^3 \gg 1]$. If their concentration is small, in addition to thermal activation, we have to take into account their probability of presence. In this case, we expect the slope of the S curve to depend on the sound wave frequency in a similar way as for type-II impurities, which is excluded.

We conclude that if cavitation is heterogeneous, it occurs on type-I impurities. Their concentration should be larger than $1/(\lambda/16)^3 \simeq 2800$ mm^{-3} (based on the 1.3-MHz sound wave), and they should be present in all the water samples we have tested. On the other hand, as we have observed zero cavitation probability at moderate negative pressures, impurities leading to a less negative threshold should always be absent, or with a concentration much less than 2800 mm^{-3}.

To give a consistent picture, the scenario of heterogeneous cavitation should also explain the observed low value of ξ (see Sec. V C). If we model the effect of type-I impurities on E_b by an effective surface tension σ_{eff}, and use the predictions of TWA replacing σ by σ_{eff}, the expression of ξ [Eq. (14)] remains unaffected, because σ cancels out in the calculation. But the factor Γ_0 is different from the value estimated for homogeneous cavitation [Eq. (2)]: the density of nucleation sites is the density of impurities n_0 instead of $1/(4\pi R_c^3/3)$, and we write

$$\Gamma_0 = n_0 \frac{k_B T}{h}. \tag{15}$$

This allows us to estimate n_0 between 1.4×10^7 mm^{-3} at 0.1 °C and 9.1×10^4 mm^{-3} at 80 °C. This is consistent with the lower bound 2800 mm^{-3}. The uncertainty on n_0 is large because of the exponential relation to ξ, but the strong temperature dependence is a robust feature, for which we do not see any obvious explanation. From the experimental P_{cav} and Eq. (3), the modified Γ_0 gives $\sigma_{eff}=14.7$ mN m^{-1} at 0.1 °C and 11.1 mN m^{-1} at 80 °C.

B. Different water samples

In this section, we discuss the results obtained for different water samples. We have used high resistivity ultrapure water, degassed, and transferred in the experimental cell under vacuum; inert materials were chosen to limit water contamination, and UV spectra of water before and after use show only a moderate increase in absorption below 240 nm. Successive experimental runs with renewed water samples give reproducible values of P_{cav}. We have also tried to vary the water sample preparation or origin. Run 9 used ultrapure water purchased from Sigma (G Chromasolv for gradient elution) and degassed with the same method as usual. Run 10 used a mineral water. We chose Speyside Glenlivet for its low minerality (dry residue at 180 °C: 58 mg L^{-1}) [61]). It also has the advantage to be packaged in glass bottles: min-

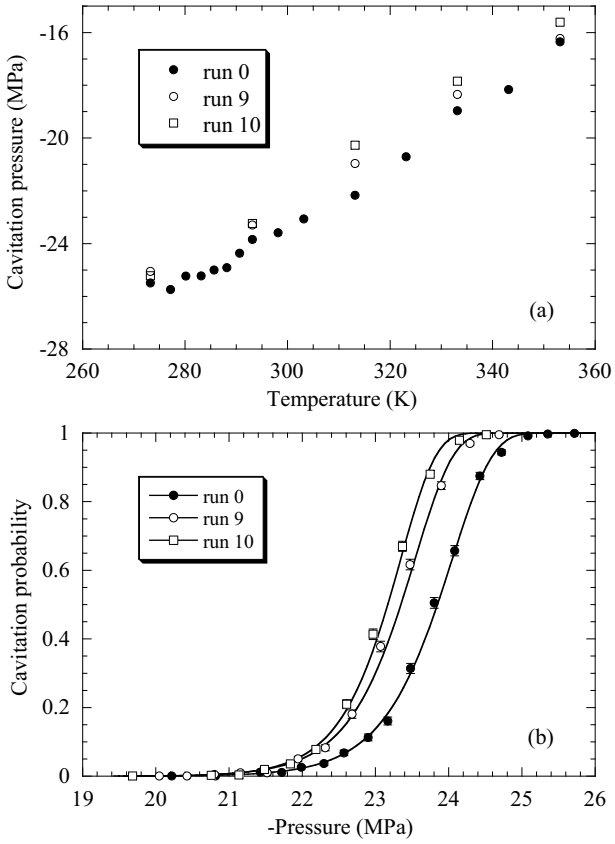

FIG. 21. Comparison between different water samples. The initial run (run 0, filled circles, as in Fig. 15) is shown for comparison. In run 9 (empty circles), we used ultrapure water from a different source (G Chromasolv for gradient elution, purchased from Sigma), and degassed with the method described in Sec. III F. In run 10 (empty squares), we used mineral water (Speyside Glenlivet, dry residue at 180 °C: 58 mg L^{-1}) (Ref. [61]), distilled in a Pyrex glassware and degassed with the same method. (a) Cavitation pressure as a function of temperature; the error bars on P_{cav} are omitted for clarity: they all have a similar amplitude (see Fig. 15). (b) Cavitation probability as a function of the minimum pressure reached in the wave. The S curves were obtained at $T=20$ °C and $P_{stat}=1.6$ MPa. The excitation voltages were converted into pressure using Eq. (11) and the value of P_{cav} shown in (a). The solid curves are fits with Eq. (12); they all give similar values of the steepness ξ: 43.3 ± 1 for run 0 ($\chi^2=2.2$), 44.6 ± 1.5 for run 9 ($\chi^2=3.9$), and 48.1 ± 1.9 for run 10 ($\chi^2=4.6$).

eral water in plastic bottles shows a strong UV absorption. In addition, we distilled the mineral water in Pyrex glassware before performing the usual degassing. All the setup was rinsed with the corresponding water before filling. We find the same P_{cav} [Fig. 21(a)] and the same cavitation statistics [Fig. 21(b)]. The UV spectra are shown in Fig. 22: the water samples coming out of the cell exhibit a larger absorbance than usual. It is difficult to trace out the origin of this pollution, but we think it occurred outside of the cell during the emptying. We have checked that it was not due to a surfactant contamination by measuring the surface tension with the Du Noüy method: we found for both samples before and after entering the cell the same value as for our reference ultrapure water, $\sigma=71\pm1$ mN m^{-1} at 25 °C.

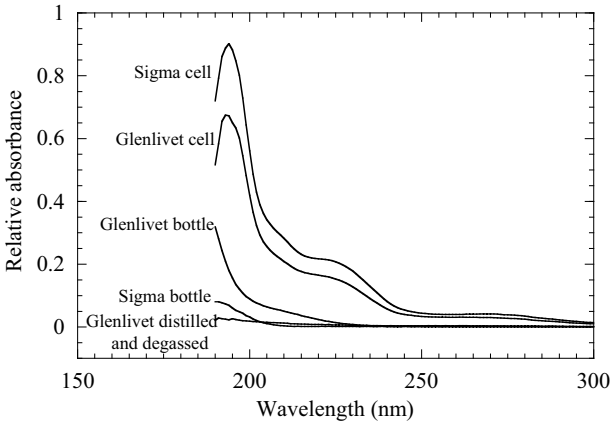

FIG. 22. UV spectra of different water samples. The labels indicate the water origin and preparation: Sigma refers to water used in run 9, and Glenlivet in run 10. Bottle is relative to the UV spectrum of water directly coming out of the commercial bottle, whereas cell refers to the water coming out of the cell at the end of the run. We also show the spectrum of Glenlivet water after distillation and degassing: these steps decrease the UV absorbance.

In order to investigate the role of impurities, we also performed experiments in *dirty* water. The cavitation voltage in tap water, measured in an open glass container, was found to be slightly larger than the one of ultrapure water in the same conditions. This effect is reduced if we cover the transducer with an insulating varnish: it is presumably due to the higher conductivity of tap water which reduces the transducer efficiency. Figure 23 shows the comparison between S curves obtained for tap and ultrapure water and normalized by the respective cavitation voltages. This normalization assumes

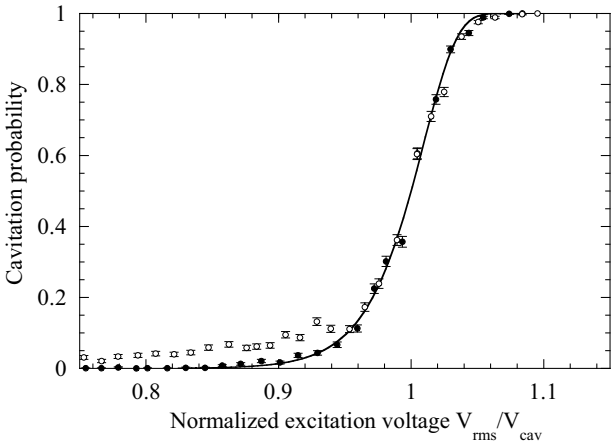

FIG. 23. Cavitation probability as a function of the excitation voltage normalized to the cavitation voltage. Full (respectively, empty) circles stand for ultrapure (respectively, tap) water. The data were recorded at room temperature in an open Pyrex glass container. Each point corresponds to 1000 repeated bursts. The solid line is a fit of the data for ultrapure water with Eq. (9). The center of these S curves are similar, but the foot for tap water is much broader than for ultrapure water. This indicates the presence in tap water of a broad distribution of dilute impurities triggering cavitation at pressures less negative than the cavitation pressure of ultrapure water.

that the 50% probability threshold is the same in both samples; this is supported by the similarity of the centers of the S curves. The low probability parts of the curves are strikingly different: ultrapure water goes smoothly to zero probability, whereas tap water gives a long tail with finite probability. This shows that our experiment is sensitive to the numerous impurities present in tap water, some of which trigger cavitation at moderate negative pressure. It shows also that the distribution of such impurities is sufficiently broad and dilute to leave the narrow center of the S curves unaffected. This means that either our experiment reaches the homogeneous cavitation limit of water, or there are very different kinds of impurities: dilute, moderate cavitation pressure impurities that can be removed by usual water purification, and a more abundant quantity of type-I impurities (see Sec. VI A). The latter have to be exceptionnaly calibrated and ubiquitous to explain the identical P_{cav} and statistics between different runs and samples. We have also investigated the cavitation threshold of water saturated with different gases (helium, nitrogen, and acetylene, which have a relative solubility in water 1:1.7:106 at 20 °C). This was done in sealed cells with a gas handling system. The cavitation voltage varied only by a few percent compared to degassed ultrapure water.

The most important point is that, if impurities are responsible for our results, all the water samples tested must have the same impurities in sufficient concentration. In the inclusion case, we shall recall that cavitation pressures fall in a narrow range at high temperature, but exhibit a large scatter at low temperature; only the largest negative pressures are reported (see Sec. II E). Angell and his group attribute the scatter to heterogeneous nucleation, and its source to "possibly surfactant molecules cluster destroyed by annealing at the higher temperatures" (in excess of 400 °C). At low temperature, the impurities should have a low enough concentration to be absent from some of the inclusions, where homogeneous nucleation would thus take place; using the inclusion volume from Table I, this gives a typical concentration of one impurity per inclusion: $n_0 \simeq 1/(4.2 \times 10^{-6}\ \mathrm{mm}^3) = 2.4 \times 10^5\ \mathrm{mm}^{-3}$, larger than the threshold at which our method becomes sensitive to impurities ($2.8 \times 10^3\ \mathrm{mm}^{-3}$, see Sec. VI A). The same remark applies to all the experiments involving larger liquid volumes than the inclusions, and is able to explain why they all obtain less negative cavitation pressures. It would be interesting to check this issue by exposing water to high temperatures before its use in our experiment. However, this presents some technical problems in the design of the cell; in addition, the Curie point of the piezoelectric material is 300 °C: water should then be heated outside of the cell, or the transducer repoled after thermal cycling.

We now turn to the other reason proposed to understand the discrepancy between the present work and the inclusion work: (ii) error in the pressure estimate in the inclusion work.

C. Pressure calibration in the inclusion work and the equation of state of water

How reliable is the pressure estimate in the inclusion work? In this method, the quantity which is measured is the cavitation *temperature*, from which the pressure is deduced from the known liquid density and the use of an EOS extrapolated in the negative pressure range. Alvarenga *et al.* [32] have shown that the assumption of an inclusion of constant volume (required to know the liquid density) was not always reliable. To estimate P_{cav}, they rather used the measured change in sound velocity c before and after nucleation, and found values beyond −100 MPa at room temperature. However, they still rely on an extrapolated EOS: they assume $(dc/dP)_T$ to keep a constant value, equal to that at liquid-vapor equilibrium.

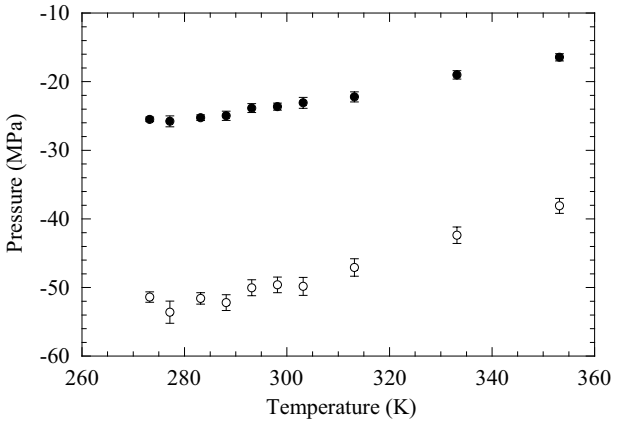

FIG. 24. Speculated spinodal pressure as a function of temperature. The values of the spinodal pressure (empty circles) were deduced from the cavitation pressures (filled circles) and steepness of the S curves (see Fig. 17) measured in run 0.

One possibility would then be that the extrapolated EOS are wrong: thermodynamic properties of water should then exhibit dramatic changes in a narrow range beyond this value to make all data compatible. This could happen, for example, if the spinodal pressure P_s was much less negative than expected from Speedy's extrapolations or molecular dynamics simulations (see Sec. I A). Let us try to make this speculation more quantitative. If cavitation in our experiments is homogeneous, then we have access to two quantities related to the EOS: the energy barrier and its slope at P_{cav}. Indeed, we write

$$E_b(P_{cav}) = k_B T \ln\left(\frac{\Gamma_0 V \tau}{\ln 2}\right) \simeq 47.5 k_B T \tag{16}$$

taking for Γ_0 the value from Eqs. (2) (with $R_c = 1$ nm) and for $V\tau$ the value from Eq. (8). The slope is given by

$$\left(\frac{\partial E_b}{\partial P}\right)_{P_{cav}} = -\frac{\xi k_B T}{P_{cav}} \tag{17}$$

which ranges from 500 to 780 K MPa^{-1} from 0.1 to 80 °C (with the values of ξ from Fig. 17). By definition, $E_b(P_s) = 0$. To locate P_s, we extrapolate linearly E_b to zero using the above values (Fig. 24). To get an idea of the accuracy of such an extrapolation, we can look at the curve $E_b(P)$ calculated with DFT [2]: it is convex, and nearly linear in the relevant range of E_b. We thus expect the actual P_s to be slightly more negative than the extrapolated value.

The spinodal proposed is much less negative than previous estimates (around −50 instead of −200 MPa at 300 K). Although surprising, it is not impossible, because of the possible uncertainties in the interparticle potential used in molecular dynamics simulations, or in the lengthy extrapolations of $P(\rho)$ involved in Speedy's EOS. In this alternative interpretation, the observed temperature dependence of ξ is simply related to the temperature dependence of the EOS.

VII. CONCLUSION

We have focused short bursts of high frequency ultrasonic waves to study cavitation in water. A detailed experimental procedure was followed to insure cleanliness of the water sample. Statistics of cavitation could be measured with high accuracy, allowing a clear definition of the cavitation threshold. We have used two independent methods to calibrate the negative pressure reached in the wave, and found them to be in excellent agreement with each other. This allowed us to measure the temperature dependence of the cavitation pressure. Our results were proven to be highly reproducible. We have found a cavitation pressure that increases monotonically with increasing temperature, from −26 MPa at 0.1 °C to −17 MPa at 80 °C.

Our values of the cavitation pressure are among the most negative ones, with the only exception of those obtained in the work on mineral inclusions. In order to understand this discrepancy, we propose two experimental checks. On one hand, further efforts should be made to improve the purity of water. We have already taken many precautions in this direction, and explained that the agreement of our results with previous studies, their reproducibility, and the statistics of cavitation disfavor the assumption that nucleation occurs on impurities in our experiment. Nevertheless, a difference remains between the inclusion work and others, including ours. During the making of inclusions, water is brought to high temperature and pressure: it would be interesting to check the effect of this procedure on cavitation pressures obtained by our method. On the other hand, the inclusion work lacks a direct measurement of the cavitation pressure, because it has to rely on the use of an extrapolated EOS. All results could be made compatible if the EOS of water was much different from what has been admitted up to now: in particular, the spinodal pressure could be much less negative than previously thought (around −50 instead of −200 MPa at 300 K). It is necessary to add experimental information on the EOS of water at large negative pressure: for this, we plan to combine our acoustic method to produce negative pressure with optical measurements to measure independently the density and speed of sound in the metastable liquid.

ACKNOWLEDGMENTS

We thank A. Berthelot, V. Fourmond, B. Haas, and R. Melet for their participation at various stages of the experiment. We thank E. Perez for providing us with ultrapure water, A. Boudaoud, C. Guthmann, L. Mercury, R. Pecha, and E. Rolley for helpful discussions, and C. Herrmann, G. Narcy, and J. Quintas for technical assistance. We are grateful to M. McKenna and B. B. Chick from Ritec Inc. for their help and advice. Support from ANR Grant No. 05-BLAN-0084-01 and Grant No. JC05-48942 is acknowledged.

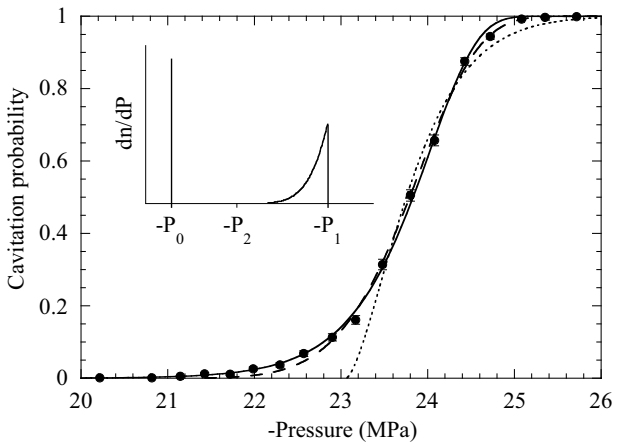

FIG. 25. Cavitation probability as a function of the minimum pressure reached in the wave. The data points are the same as in Fig. 9. The excitation voltage has been converted into pressure using Eq. (11) and $P_{cav}=-23.845$ MPa. Only pressures between −20 and −26 MPa are shown. The solid line is a fit with Eq. (12). The best fit gives $-P_{cav}=23.847\pm0.019$ MPa and $\xi=43.3\pm1$ with $\chi^2=2.2$. The inset shows the two distributions of type-II impurities tested (see Appendix B). Equation (B6) (corresponding to the monodisperse distribution) does not allow a good fit; the dotted line is drawn with $P_0=-23$ MPa and $n_0\lambda^3=600$ to pass through the high probability data. The dashed line is a fit with Eq. (B8); P_2 was set to −20 MPa, and the best fit was obtained for $\alpha=5$: it gives $n_0\lambda^3/(P_2-P_1)^6=(0.31\pm0.01)$ MPa^{-6} and $\chi^2=3.7$.

APPENDIX A: ACCURACY OF THE STATISTICS OF CAVITATION

As explained in Sec. IV B, our method allows us to repeat many cavitation experiments under the same conditions. This determines accurately the probability of cavitation. We have measured the cavitation probability vs excitation voltage curves (S curves). Once the pressure has been calibrated with the static pressure method (Sec. IV D), the excitation voltage is converted into minimum pressure reached in the wave. The S curves are well fitted by the relation expected for thermally activated cavitation [Eq. (12)]. Here we estimate the error bars on the fitting parameters P_{cav} and ξ. In the absence of other noise, the uncertainty on the probability Σ comes from the finite number of repeated bursts used for its measurement, N_b; the standard deviation SD is given by the binomial law: $\sigma_\Sigma=\sqrt{N_b\Sigma(1-\Sigma)}$. This can be used in the fitting procedure to give a normalized mean-square deviation χ^2 and error bars on the fitting parameters. The fit has to be limited to the region where Σ is different from 0 and 1, in order to keep σ_Σ nonzero. For instance, applying this procedure to the data in Fig. 25 gives $\chi^2=2.2$, $P_{cav}=23.85\pm0.016$ MPa, and $\xi=43.3\pm1$.

However, we must also account for the noise on the excitation voltage V_{rms} applied to the transducer. The value of V_{rms} is recorded for each burst; when the output level of the

TABLE III. Characterization of the fitting results of the simulated S curves. The parameters used in the simulation were $-P_{cav,0}=24$ MPa, $\xi_0=43$, $-P_m=21.7$ MPa, $-P_M=25.0$ MPa, $\sigma_P=0.1$ MPa, $N_{simul}=1000$, $N_{pts}=15$, and $N_b=1000$.

	Average	Skewness	Standard deviation	Average asymptotic standard errors
$-P_{cav}$ (MPa)	24.003	0.111	0.0093	0.0093
ξ	42.75	0.069	0.629	0.617
χ^2	1.064	1.51	0.448	

amplifier is set to a constant value, we observe that V_{rms} follows a normal distribution: typical values are 0.6 V SD for a 150-V average. The corresponding average value and SD of P_{min} are deduced from the affine relation Eq. (11) (typically a 0.1 MPa SD for a −25 MPa average). The noise on P_{min} tends to enlarge the S curve and decrease the steepness ξ. To estimate this effect we have performed a numerical experiment in the following way. We assume that cavitation is a stochastic phenomenon occurring with the probability given by Eq. (12), with $P_{cav}=P_{cav,0}$ and $\xi=\xi_0$. We choose N_{pts} values of P_{min} between P_m and P_M. For each P_{min}, we take N_b values P_i of a normal distribution with an average P_{min} and a SD σ_P; for each P_i, a cavitation event occurs with a probability $\Sigma(P_i)$. The average of the P_i and of the number of cavitation events gives one data point of an S curve. N_{simul} S curves are simulated this way, and fitted with Eq. (12). This leads to N_{simul} pairs of fitting parameters, with their asymptotic standard error bars ($1-\sigma$ confidence interval), and values of χ^2. Table III gives the statistical properties of the results; the simulation was performed using input values close to the experimental ones (see caption of Table III). It can be seen that P_{cav} is correctly obtained by the fit, whereas ξ is slightly underestimated, as expected. Nevertheless, the noise on the excitation voltage is sufficiently small compared to the width of the S curves to give reliable fitting parameters, with the actual values lying inside the error bars. Therefore we can use the fitting parameters and asymptotic standard error bars obtained by fitting the experimental data weighed by the SD on the probability given by the binomial law. For example, the best fit of the central region of the S curve shown in Fig. 25 gives $-P_{cav}=23.847\pm0.019$ MPa and $\xi=43.3\pm1$ with $\chi^2=2.2$.

In Sec. V C, we have emphasized that the measured ξ (around 40) was significantly lower than the value predicted by TWA (around 95). To check that this is not an artifact due to an enlargement of the width of the S curve by the experimental noise, we have performed simulations similar to the above ones, assuming $\xi=95$: the noise does enlarge the S curve, but only slightly: we find a fitting value of $\xi=90.3\pm1.3$. The artifact is ruled out and the discrepancy confirmed.

APPENDIX B: CAVITATION PROBABILITY ON TYPE-II IMPURITIES

We have discussed the role of type-II impurities in Sec. VI A. We give here the details of the calculation of the cavitation probability. Type-II impurities have a deterministic effect on cavitation: it occurs if and only if the impurity is present at a position where the pressure exceeds a threshold defined by the impurity. Let us call dn/dP the distribution of these thresholds: the concentration of impurities with a threshold between P and $P+dP$ is $(dn/dP)dP$. We then calculate the cavitation probability at a time where the pressure reaches its minimum P_{min} at the focus; if the pressure at a point $\mathbf{r}$ is $P(\mathbf{r})$, we find

$$\Sigma(P_{min}) = 1 - \exp\left(-\int_V d\mathbf{r}\int_{P(\mathbf{r})}^{P_{sat}} dP\frac{dn}{dP}\right), \tag{B1}$$

where V is the total volume of liquid. In practice, because the sound wave is sharply focused, V can be replaced by the volume of the focal region.

The simplest distribution is that of impurities all having the same threshold P_0:

$$dn/dP = n_0\delta(P - P_0) \tag{B2}$$

where n_0 is the concentration of impurities.This situation is experimentally realized in the case of electron bubbles in liquid helium [62]. Then

$$\Sigma(P_{min}) = 1 - \exp[-n_0 V(P < P_0|P_{min})] \tag{B3}$$

with $V(P<P_0|P_{min})$ the volume in which the pressure is below the threshold P_0, provided the minimum pressure is P_{min}. At this stage we need an expression for $P(\mathbf{r})$: we could use the map of the acoustic field experimentally determined (see Sec. IV C), but the calculation becomes simpler if we take the approximation of a focused spherical wave:

$$P(\mathbf{r}) = P_{min}\frac{\sin(kr)}{kr}, \tag{B4}$$

where $r=|\mathbf{r}|$ and $k=2\pi/\lambda$. If we introduce r_0 such that $P(r_0)=P_0$, we find

$$\Sigma(P_{min}) = 1 - \exp\left(-n_0\frac{4}{3}\pi {r_0}^3\right). \tag{B5}$$

An expansion in power of $\epsilon=1-(P_0/P_{min})$ gives

$$\Sigma(P_{min}) = 1 - \exp\left[-n_0\lambda^3\frac{\sqrt{6}}{\pi^2}\epsilon^{3/2}\left(1+\frac{9}{20}\epsilon+O(\epsilon^2)\right)\right]. \tag{B6}$$

However, Eq. (B6) fails to give a good fit to the experimental data, because of the pronounced inflection of the S curves. This leads us to consider more elaborated distributions. We have tried power laws, starting at a pressure P_2 and

TABLE IV. Characterization of the fitting results of the simulated S curves. The parameters used in the simulation were $\alpha=5$, $-P_2=20$ MPa, $n_0\lambda^3/(P_2-P_1)^6=0.31$ MPa^{-6}, $-P_m=22.1$ MPa, $-P_M=25.0$ MPa, $\sigma_P=0.1$ MPa, $N_{simul}=1000$, $N_{pts}=15$, and $N_b=1000$.

	Average	Skewness	Standard Deviation	Average asymptotic standard errors
$n_0\lambda^3/(P_2-P_1)^6$ (MPa^{-6})	0.3090	0.118	0.0047	0.0046
χ^2	1.061	0.791	0.397	

truncated at a pressure P_1 (see inset of Fig. 25):

$$dn/dP = \frac{\alpha n_0}{(P_2-P_1)^\alpha}(P_2-P)^{\alpha-1}. \tag{B7}$$

This gives

$$\Sigma(P_{min}) = 1-\exp\left\{-n_0\lambda^3\left(\frac{-P_2}{P_2-P_1}\right)^{\alpha+1}K(\alpha)\epsilon^{3/2} \times [1+L(\alpha)\epsilon+O(\epsilon^2)]\right\} \tag{B8}$$

with

$$K(\alpha) = \left(\frac{3}{2\pi}\right)^{3/2}\frac{\Gamma(\alpha+2)}{\Gamma\left(\alpha+\frac{7}{2}\right)} \tag{B9}$$

and

$$L(\alpha) = \frac{7}{4}+\frac{13}{10}\alpha-\frac{3}{10}\frac{(\alpha+1)(\alpha+5)}{\alpha+\frac{7}{2}}. \tag{B10}$$

As can be seen from Eq. (B8), P_2 and $n_0\lambda^3/(P_2-P_1)^{\alpha+1}$ are dependent parameters. Therefore, to fit the data, we fix P_2 at a value chosen as a pressure just above the lowest negative pressure at which a nonzero probability is observed in the experiment, and find the best fit value for $n_0\lambda^3/(P_2-P_1)^{\alpha+1}$. To estimate the quality of the fit and the uncertainty, we have performed numerical experiments as explained in Appendix A, but now with $\Sigma(P_{min})$ given by Eq. (B6). The results of the simulation are reported in Table IV. As in Appendix A, we find that the actual value of $n_0\lambda^3/(P_2-P_1)^{\alpha+1}$ lies within the asymptotic error bars given by the fit. We will take this value for the uncertainty in a fit of experimental data. An example is given in Fig. 25; the best fit, obtained with $\alpha=5$, is satisfactory ($\chi^2=3.7$).

[1] P. G. Debenedetti, *Metastable Liquids* (Princeton University Press, Princeton, 1996), and references therein.
[2] F. Caupin, Phys. Rev. E **71**, 051605 (2005).
[3] R. Becker and W. Döring, Ann. Phys. **24**, 719 (1935).
[4] Y. B. Zel'dovich, Zh. Eksp. Teor. Fiz. **12**, 525 (1942).
[5] J. C. Fisher, J. Appl. Phys. **19**, 1062 (1948).
[6] M. S. Pettersen, S. Balibar, and H. J. Maris, Phys. Rev. B **49**, 12062 (1994).
[7] R. J. Speedy, J. Phys. Chem. **86**, 982 (1982).
[8] P. H. Poole, F. Sciortino, U. Essmann, and H. E. Stanley, Nature (London) **360**, 324 (1992).
[9] S. Sastry, P. G. Debenedetti, F. Sciortino, and H. E. Stanley, Phys. Rev. E **53**, 6144 (1996).
[10] M. Yamada, S. Mossa, H. E. Stanley, and F. Sciortino, Phys. Rev. Lett. **88**, 195701 (2002).
[11] G. S. Kell, Am. J. Phys. **51**, 1038 (1983).
[12] D. H. Trevena, J. Phys. D **17**, 2139 (1984).
[13] C. T. Avedisian, J. Phys. Chem. Ref. Data **14**, 695 (1985).
[14] T. G. Leighton, *The Acoustic Bubble* (Academic Press, London, 1994).
[15] F. Caupin and E. Herbert, C. R. Phys. (to be published).
[16] M. Berthelot, Ann. Chim. Phys. **30**, 232 (1850).
[17] S. J. Henderson and R. J. Speedy, J. Phys. E **13**, 778 (1980).
[18] S. J. Henderson and R. J. Speedy, J. Phys. Chem. **91**, 3062 (1987).
[19] K. Hiro, Y. Ohde, and Y. Tanzawa, J. Phys. D **36**, 592 (2003).
[20] O. Reynolds, Mem. Manch. Lit. Phil. Soc. **7**, 1 (1882).
[21] L. J. Briggs, J. Appl. Phys. **21**, 721 (1950).
[22] C. Wurster, M. Köhler, R. Pecha, W. Eisenmenger, D. Suhr, U. Irmer, F. Brümmer, and D. Hülser, in *Proceedings of the 1st World Congress on Ultrasonics, Berlin, 1995*, edited by J. Herbertz (Universität Duisburg-Essen, Duisburg, 1995), Part 1, p. 635.
[23] J. Staudenraus and W. Eisenmenger, Ultrasonics **31**, 267 (1993).
[24] R. Pecha (private communication).
[25] W. J. Galloway, J. Acoust. Soc. Am. **26**, 849 (1954).
[26] M. Greenspan and C. E. Tschiegg, J. Res. Natl. Bur. Stand., Sect. C **71**, 299 (1967).
[27] R. D. Finch, J. Acoust. Soc. Am. **36**, 2287 (1964).
[28] W. J. Galloway (private communication to R. D. Finch, Ref. [6] of Ref. [27]).
[29] J. L. Green, D. J. Durben, G. H. Wolf, and C. A. Angell, Science **249**, 649 (1990).
[30] Q. Zheng, D. J. Durben, G. H. Wolf, and C. A. Angell, Science **254**, 829 (1991).
[31] V. P. Skripov, in *Water and Steam*, edited by J. Straub and K. Scheffer (Pergamon, Elmsford, NY, 1980).
[32] A. D. Alvarenga, M. Grimsditch, and R. J. Bodnar, J. Chem. Phys. **98**, 8392 (1993).
[33] Q. Zheng, J. Green, J. Kieffer, P. H. Poole, J. Shao, G. H. Wolf, and C. A. Angell, in *Proceedings of the NATO Advanced Research Workshop on Liquids Under Negative Pressure, Budapest, 2002*, NATO Science Series, Series II: Mathematics,

Physics and Chemistry, Vol. 84, edited by A. R. Imre, H. J. Maris, and P. R. Williams (Kluwer, Dordrecht, 2002), p. 33.
[34] M. Takahashi, E. Izawa, J. Etou, and T. Ohtani, J. Phys. Soc. Jpn. **71**, 2174 (2002).
[35] H. W. Strube and W. Lauterborn, Z. Angew. Phys. **29**, 349 (1970).
[36] C. G. Wohl *et al.*, Rev. Mod. Phys. **56**, S1 (1984).
[37] R. A. Roy, S. I. Madanshetty, and R. E. Apfel, J. Acoust. Soc. Am. **87**, 2451 (1990).
[38] C. K. Holland and R. A. Roy, J. Acoust. Soc. Am. **88**, 2059 (1990).
[39] C. X. Deng, Q. Xu, R. E. Apfel, and C. K. Holland, J. Acoust. Soc. Am. **100**, 1199 (1996).
[40] J. A. Nissen, E. Bodegom, L. C. Brodie, and J. S. Semura, Phys. Rev. B **40**, 6617 (1989).
[41] H. Lambaré, P. Roche, S. Balibar, H. J. Maris, O. A. Andreeva, C. Guthmann, K. O. Keshishev, and E. Rolley, Eur. Phys. J. B **2**, 381 (1998).
[42] F. Caupin and S. Balibar, Phys. Rev. B **64**, 064507 (2001).
[43] NIST Chemistry WebBook, Thermophysical Properties of Fluid Systems, http://webbook.nist.gov/chemistry/fluid/
[44] A. D. Bangham and M. W. Hill, Nature (London) **237**, 408 (1972).
[45] L. J. Heidt and L. Ekstrom, J. Am. Chem. Soc. **79**, 1260 (1957).
[46] G. W. Willard, J. Acoust. Soc. Am. **25**, 669 (1953).
[47] L. A. Crum and J. B. Fowlkes, Nature (London) **319**, 52 (1986).
[48] J. B. Fowlkes and L. A. Crum, J. Acoust. Soc. Am. **83**, 2190 (1988).
[49] A. A. Atchley, L. A. Frizzell, R. E. Apfel, C. Holland, S. Madenshetty, and R. Roy, Ultrasonics **26**, 280 (1988).
[50] F. Caupin and V. Fourmond, in *Proceedings of the NATO Advanced Research Workshop on Liquids Under Negative Pressure, Budapest, 2002*, NATO Science Series, Series II: Mathematics, Physics and Chemistry, Vol. 84, edited by A. R. Imre, H. J. Maris, and P. R. Williams (Kluwer, Dordrecht, 2002), p. 307.
[51] D. Messino, D. Sette, and F. Wanderlingh, J. Acoust. Soc. Am. **35**, 1575 (1963).
[52] C. Appert, C. Tenaud, X. Chavanne, S. Balibar, F. Caupin, and D. d'Humières, Eur. Phys. J. B **35**, 531 (2003).
[53] X. Chavanne, S. Balibar, F. Caupin, C. Appert, and D. d'Humières, J. Low Temp. Phys. **126**, 643 (2002).
[54] H. B. Briggs, J. B. Johnson, and W. P. Mason, J. Acoust. Soc. Am. **19**, 664 (1947).
[55] W. H. Press, B. P. Flannery, S. A. Teukolsky, and W. T. Vetterling, *Numerical Recipes* (Cambridge University Press, Cambridge, England, 1989), Chap. 14.2.
[56] E. Herbert and F. Caupin, J. Phys.: Condens. Matter **17**, S3597 (2005).
[57] E. Ruckenstein and R. Nagarajan, J. Phys. Chem. **79**, 2622 (1975).
[58] F. E. Fox and K. F. Herzfeld, J. Acoust. Soc. Am. **26**, 984 (1954).
[59] M. Strasberg, J. Acoust. Soc. Am. **31**, 163 (1959).
[60] A. A. Atchley and A. Prosperetti, J. Acoust. Soc. Am. **86**, 1065 (1989).
[61] Speyside Glenlivet, http://www.speysideglenlivetwater.com/
[62] J. Classen, C.-K. Su, M. Mohazzab, and H. J. Maris, Phys. Rev. B **57**, 3000 (1998).